

The Pennsylvania State University
The Graduate School
College of Engineering

**COMPUTATION OF VISCOUS MULTIPHASE
HYDRODYNAMICS AND SHIP MOTIONS
DURING WAVE-SLAP EVENTS AND WAVE
EXCITED ROLL**

A Thesis in
Mechanical Engineering
by
Kevin R. Smith

©2009 Kevin R. Smith

Submitted in Partial Fulfillment
of the Requirements
for the Degree of
Master of Science

May 2009

The thesis of Kevin R. Smith was reviewed and approved* by the following:

Eric Paterson

Division Scientist, Computational Mechanics Division, Applied Research Lab

Associate Professor of Mechanical Engineering

Thesis advisor

Kendra Sharp

Associate Professor of Mechanical Engineering

Karen Thole

Department Head of Mechanical and Nuclear Engineering

Professor of Mechanical Engineering

*Signatures are on file in the Graduate School

ABSTRACT

There is a need for computational tools which can accurately predict non-linear ship motions and wave-impact loads. Lateral ship motions (roll, sway, and yaw) can be very non-linear in nature due to viscous effects and flow separation. Roll damping is especially important to predict because it is critical to the stability of a ship in waves. Roll damping is primarily due to viscous effects, which are not resolvable using potential flow methods. Wave impact loads, or “wave-slap”, can damage a ship’s hull and deck structures and the frequency and magnitude of the loads can be coupled with the ship motions. The objective of this thesis is to provide the building blocks of a computational seakeeping model which can predict the motions of a ship at sea including the effect of large amplitude waves.

A seakeeping model is made up of several fundamental building blocks or component models. The components developed and tested in the present work include a wave maker boundary condition, a non-reflecting boundary, dynamic mesh motion, and 6DOF rigid-body motion. A second order Stokes deep water wave maker boundary condition is developed and several tests are presented to study and validate the model. A non-reflecting boundary technique known as a numerical sponge layer is developed and tested to show that wave reflections can be reduced below 5% of the incoming wave amplitude. A 6DOF motion solver is developed and coupled with the pre-existing mesh motion techniques. The validity of the 6DOF model is proven using free-decay and wave-excited numerical experiments of a floating 2D rectangular box barge. Wave-impact phenomena are studied using a dam break case and a practical example of a wave impacting a floating block. Several studies are performed to examine grid dependency and scaling effects. All components are developed within the OpenFOAM platform using a fully viscous and turbulent multi-phase fluid model.

Table of Contents

List of Figures	vii
List of Tables	ix
Symbols	x
Abbreviations	xii
Acknowledgements	xiii
Chapter 1	
Introduction	1
1.1 Motivation	1
1.2 Objective	1
1.3 Approach	2
1.4 Literature Review	2
1.4.1 Ship Motions	2
1.4.2 Wave-Slap Loads	5
1.4.3 Wave Models	6
1.4.4 Non-Reflecting Boundaries	7
1.4.5 OpenFOAM	9
1.5 Agenda	10
Chapter 2	
Governing Equations and Numerical Methods	11
2.1 Governing Equations	11

2.1.1	Turbulent Multiphase Flow Model	11
2.1.2	Sponge Layer	12
2.1.3	K- ε Turbulence Model	12
2.1.4	6 Degree-of-Freedom Equations	13
2.1.5	Surface Wave Models	16
2.2	Numerical Methods	17
2.2.1	General Method of Solution of Multiphase Solver	17
2.2.2	Boundary Conditions	18
2.2.3	Finite Volume Method	19
2.2.4	Mesh Motion	19

Chapter 3

Computations		20
3.1	Prescribed Body Motion and Laminar Single-Phase Navier-Stokes Fluid Model	21
3.1.1	Oscillating Cylinder	21
3.2	Prescribed Body Motion and Free-Surface RANS	25
3.2.1	Prescribed Roll Oscillation of Tumblehome Midship Geometry	25
3.3	Free Rigid-Body Motion and Free-Surface RANS	29
3.3.1	Free-Roll of 2D Box Barge	29
3.3.2	Wave-induced Roll of 2D Box Barge	31
3.4	Deep Water Wave Model	35
3.4.1	Dependency on Basin Depth	35
3.4.2	Wave Breaking Limit	36
3.4.3	Uniform Grid Spacing Variation	39
3.5	Sponge Layer	41
3.5.1	Wave Dissipation Cases	41
3.5.2	Wave Dissipation with Expanded Grid Cells	43
3.6	Wave Slap Loads	46
3.6.1	Scaling of Impact Loads	46
3.6.2	Impact Load Grid Dependency	48

3.6.3	Wave Loads on a Fixed Structure	51
-------	---	----

Chapter 4

Summary	55
----------------	-----------

4.1	Prescribed Motion	55
-----	-----------------------------	----

4.2	Free 1DOF Motion	56
-----	----------------------------	----

4.3	Wave Model	56
-----	----------------------	----

4.4	Non-Reflecting Boundary	57
-----	-----------------------------------	----

4.5	Wave Impact Loads	57
-----	-----------------------------	----

4.6	Future Work	58
-----	-----------------------	----

Bibliography	59
---------------------	-----------

List of Figures

1.1	Components of computational model	2
2.1	Wave Basin with sponge layer	13
2.2	Body boundary	14
2.3	Boundary cell face velocity vectors	16
2.4	Wave boundary condition realisation	18
3.1	Cylinder mesh and prescribed motion description	22
3.2	Vortex shedding, $A = 0.2$, $F = 1.05$, $Re = 100$, red = positive vorticity, blue = negative vorticity	23
3.3	Oscillating cylinder results - Case 1: $A = 0.2$, $F = 0.6$ - Case 2: $A = 0.2$, F = 1.05	24
3.4	Deformed cylinder mesh	25
3.5	ONRTH sections	26
3.6	ONRTH bare hull mesh	26
3.7	ONRTH bilgekeels mesh	27
3.8	Bilge keels vortex shedding, $A = 15^\circ$, $F = 4.83$ rad/s. Red = positive vor- ticity, Blue = negative vorticity, Black line indicates free-surface	28
3.9	ONRTH bilgekeels mesh deformed. Amplitude = 30° , Frequency = 4.83 rad/s	28
3.10	2D box barge free-roll problem schematic	29
3.11	2D barge with bilge radius. (d) Initial condtns, 15° of inclination, Blue indicates water	30
3.12	Free roll decay analysis. Solid line = 0.625% bilge radius case. Dashed line = No BR case.	32
3.13	2D box barge wave-excited roll problem schematic	33

3.14	2D barge grid with high fidelity for wave propagation	33
3.15	Magnification factors	34
3.16	Deep-water wave grids	36
3.17	Deep water wave propagation dependency	37
3.18	Example of spilling wave (Rapp and Melville, 1990)	38
3.19	Waterfall plots of cases above and below experimental breaking limit for deep water spilling breakers	39
3.20	Grid spacing study	40
3.21	Section of wave tank mesh	41
3.22	Reflection coefficients	43
3.23	Water fall plots showing cases of varying beach parameters and no sponge layer	44
3.24	Region of mesh with active sponge layer	44
3.25	Reflection coefficient along constant beach lengths with graded mesh in sponge layer zone	45
3.26	Dam break case	46
3.27	Dam break case - Pressure coefficient	47
3.28	Dam break case with constant Re , Fr	48
3.29	Dam break, uniform grid spacing	49
3.30	Dam break, graded mesh near block	50
3.31	Dam break, graded mesh	51
3.32	Wave-slap problem schematic	51
3.33	Overall and close-up views of the fixed block mesh	52
3.34	Wave impact flow evolution	53
3.35	Impact pressure	54

List of Tables

2.1	OpenFOAM boundary conditions	19
3.1	Boundary conditions	21
3.2	Cylinder test cases	23
3.3	ONRTH midship boundary conditions	27
3.4	Free decay results comparison	31
3.5	Boundary conditions for wave-induced box barge cases	34
3.6	Wave parameters	34
3.7	Deep water wave parameters	35
3.8	Wave steepness parameters	38
3.9	CPU time for sea state 5 cases	40
3.10	Wave basin boundary conditions	42
3.11	Scaling of impact pressure	47
3.12	Scaling of impact pressure with constant Re, Fr	48
3.13	Impact times	49
3.14	Impact times	50
3.15	Boundary conditions of fixed structure wave impact case	52

Symbols

A	Wave amplitude
b	Damping coefficient
E_{ij}	Strain rate tensor
F	Force on body
GM_T	Metacentric height
g	Acceleration due to gravity
H	Wave height
h	Depth of channel
I_x, I_y, I_z	Moment of inertia components
K_1	Slope of curve-of-extinction
K	Turbulent kinetic energy
k	Wave number
M	Sponge layer initial/final line slope
M_O	Total moment acting on the body
Re	Reynolds number
T_ϕ	Period of roll
U	Velocity
u_i	Fluid velocity
V_c	Wave phase velocity
x_{start}	Starting location of sponge layer
γ	Phase fraction
Δ	Displacement of floating body
δ_{ij}	Kroneker delta function
ε	Turbulent dissipation rate
η	Wave surface elevation
λ	Wave length

ν_e	Eddy viscosity
ν	Kinematic viscosity of fluid
$\nu_{d,max}$	Maximum value of dissipation function
$\nu_d(x)$	Artificial dissipation function
ρ	Density
τ_{ij}	Reynolds stress tensor
ω	Angular velocity
ω_w	Wave circular frequency

Abbreviations

CFD	Computational Fluid Dynamics
CPU	Central Processing Unit
DOF	Degrees-of-Freedom
DTMB	David Taylor Model Basin
EFD	Experimental Fluid Dynamics
FEM	Finite Element Method
FFT	Fast Fourier Transform
FPSO	Floating Production Storage and Offloading vessel
FVM	Finite Volume Method
ONR	Office of Naval Research
OpenFOAM	Open Field Operation and Manipulation
RANS	Reynolds-Averaged Navier-Stokes
VOF	Volume-of-Fluid

Acknowledgements

I would like to express my gratitude for my advisor, Dr. Eric Paterson, and acknowledge the financial support provided by NAVSEA (Contract N00024-02-D-6604, D.O. 0460), which made this thesis possible. I would also like to acknowledge Mr. Jack Lee (SEA05Z11) as my mentor and Ms. Diane Segelhorst (SEA07073R), for sponsoring and administrating the NAVSEA student scholarship. I am grateful for their support and guidance.

Chapter 1

Introduction

1.1 Motivation

There is a need for a computational tool which can accurately predict wave impact loads on ships and the motions of ships in waves. Wave impact loads can cause damage to the ship hull and deck structures, therefore computational techniques which provide an accurate estimation of the impact pressure are required. Ship motions are critical to predict because many issues are directly related. For instance, a ship can capsize due to poor dynamic stability. Platform stability is an issue for weapons launch in higher sea states. Crew and passenger comfort further motivates the characterization of ship motions. The determination of the safe operating envelope is also critical for some platforms, such as submarines that are limited to lower sea states. The accurate prediction of ship motions is an area of active research and there is strong motivation to further develop these computational technologies.

1.2 Objective

The objective of this thesis is to verify and validate the components of a CFD model which can accurately predict wave impact loads and the motions of floating bodies in waves.

1.3 Approach

A computational tool is developed which can simulate motions of floating bodies in waves. Figure 1.1 shows the components of the computational tool. The main effort is to develop, test, and validate each of the components of this computational model in the areas of floating body-motions, wave models, wave impact loads, and non-reflecting boundaries.

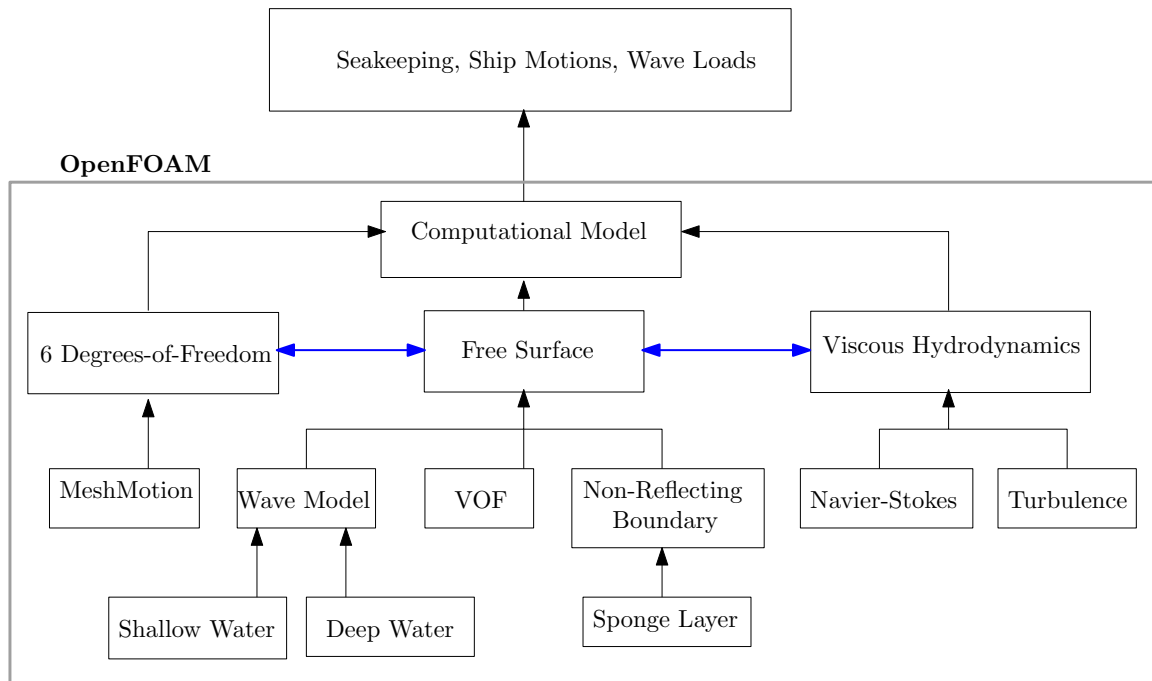


Figure 1.1: Components of computational model

1.4 Literature Review

1.4.1 Ship Motions

Linear Models and Potential Flow

Ships motions are characterized by translation and rotation in 3D space. This gives 6 degrees-of-freedom (6DOF) for surge, sway, heave, roll, pitch, and yaw. The simplest approach to the ship motions problem is to assume that the ship's response to waves will be

solutions to a 2nd order, ordinary differential equation of the form,

$$a \frac{d^2 y}{dt^2} + b \frac{dy}{dt} + cy = F(t).$$

This approach requires that the coefficients a , b , and c and the exciting force $F(t)$, be determined experimentally or from some other computational method such as strip theory. This model assumes a linear response to waves which requires the assumption of small amplitude motions. The most common occurrences, which conflict with this assumption, are during any resonance situation, eg. roll resonance in beam seas, pitch resonance, and heave resonance (Beck et al., 1989; Bhattacharyya, 1978).

The use of strip theory allows relatively good prediction of longitudinal motions (surge, heave, and pitch) of slender shaped bodies in waves. A ship is broken down into 2D slices or stations, at which point a computation of the inertia, damping, restoring coefficients and exciting force amplitudes can be obtained for each slice. Coefficients for the entire ship are then calculated. Potential flow analysis has been used for this purpose for many years with proven success. However, this approach will not resolve any viscous effects, which can play an important role during lateral motions (roll, sway, yaw). For instance, this method would have difficulty accurately predicting the roll decay of a ship at forward speed. Strip theory also does not necessarily give accurate results for ships at high forward speeds and ships with unconventional geometry. (Beck et al., 1989)

Telste and Belknap (2008), studied the current state-of-the-art, free-surface potential codes capable of predicting loads on ships due to wave excitation. This was done by performing a set of computations across a selection of codes and then comparing the results against each other. The full-scale, DTMB Models 5613 (Tumblehome), and 5514 were used in these computations. The report concluded that the results of the codes were not consistent due to code immaturity. Issues such as numerical stability and signal noise were also evident in the results. The report showed that the inherent non-linearity of the problems essentially limits the codes' scope of application.

Viscous Models

Another approach to the ship motions problem is to couple 6DOF motions with fully viscous-fluid models. By making use of high powered computer clusters, large scale computations can be solved in reasonable amounts of time.

Sato et al. (2000) performed a simulation of Wigley and Series 60 hulls in head seas (180° between wave propagation direction and ship velocity vector) allowing 2DOF for pitch and heave. The code used the Navier-Stokes equations to solve for the flow field and a marker-density-function method to calculate the free surface. The computational domain was fixed with the body during the motions. The pitching motion predicted by the simulation compared well with experiment, although there were some minor discrepancies with the heave motion data. This paper made a good first step to show that a viscous, multiphase simulation can predict ship motions accurately.

Wilson et al. (2006) showed that a RANS technique can be used to predict the viscous roll motion of a ship with forward speed. The computational solver allowed for overset grid. Each degree-of-freedom could be chosen to be either predicted by the equations of motion or prescribed by an arbitrary function. The free-surface was tracked using a conforming grid. The roll decay of a DTMB Model 5512 hull with forward speed was computed and compared well the experimental results. The model accurately predicted the natural roll frequency and roll decay rate. This computation shows that non-linear problems can be accurately solved using a RANS approach.

Carrica et al. (2007) performed simulations of a DTMB Model 5512 hull with forward speed in regular head waves allowing pitch and heave. An unsteady RANS approach was used with a single-phase level set method to capture the free surface. An overset grid technique was used to allow the rigid-body motion of the ship due to wave excitation. An advantage to using an overset method is that large amplitude motions can be realized because grid deformation is not required. The results for the sinkage, trim, pitch, and heave responses compared well with experiment. A limitation of using the single-phase level set method is that no flow fields are resolved for air.

It is evident that a computational approach that allows for viscous effects can be a

powerful tool and is a viable solution with today's computer technology.

1.4.2 Wave-Slap Loads

Various techniques have been used to predict the loads induced by a wave impact. Greco et al. (2006) used a potential-flow technique to model a wave-slap event on a 2 dimensional ship bow and deck with zero forward speed in head seas. The initial water-impact event is divided down into 3 phases: an acoustic phase, a blunt-impact phase, and a wedge-impact phase. The maximum pressure in the acoustic phase is estimated from the acoustic pressure, $p = \rho c_{s,w} V$, where ρ is the water density, $c_{s,w}$ is the speed of sound in water, and V is the impact velocity. The event is characterized by very high pressures on the order of 6 MPa for a very short duration of 10^{-5} seconds. Greco concludes that although the pressure is high, the load time is very short and therefore, this phase has a minimal effect on the structure. The blunt impact phase has a longer duration, but the load is on the order of 37 kPa. The wedge-impact phase is the point in time at which water impacts the deck of the boat and has even lower pressures on the order of 18 kPa as estimated by the Wagner method. After the flow separates during the wedge impact it coalesces and propagates on the ship deck. At this point the flow is similar to a dam break type problem and potential flow can be used up until the flow separates again. The results from the potential flow calculation match experiment well. However, after the water breaks from impacting a structure, the computation was halted and no numerical results exist during that time. Also, during that time, higher pressures were recorded in the experiment. This study provides useful insight into the different phases of a water impact, but shows the weaknesses of potential flow analysis.

Malenica and Korobkin (2007) looks into using the Generalized Wagner Model (GWM), the Modified Logvinovich Model (MLM), and the 3D Generalized von-Karman Model (GvKM), to predict water impacts on 3D geometries. GWM and MLM are restricted to 2D geometries and in general the techniques show good agreement with experiments. The GWM and MLM methods can be applied to 3D problems by choosing 2D sections or cuts of a 3D geometry. The results of the computations were compared against each other and showed good consistency, however no such comparison with experiment was presented.

MLM was shown to be a slightly more efficient computation, using less CPU time. The GvKM was applied to a passenger ship undergoing forced water entry, also known as a drop test. The computational results of the vertical force on the ship bow matched experiment reasonably well. More development is needed since these techniques have been applied only to drop tests. Wave impacts and ship motions are not taken into account with these methods.

Shibata and Koshizucka (2007) used a Lagrangian particle method to perform a simulation in which a 3D representation of a ship bow is impacted by a regular wave. Pressure data was taken on the forecastle and compared with experiment. The computational results of the pressure did not compare well with the experiment and had an error of about 50%. However the calculated shipping water propagation was predicted reasonably well. Shibata concluded that a Lagrangian particle method applied to a wave impact problem requires very high spatial resolution to obtain accurate results for impact pressures.

Kleefsman (2005) performed a computation of a 3D dam break case in which a block was impacted by water. A RANS flow model and a VOF algorithm were used to perform the simulation. The results of both the water propagation and the water-impact loads compared well with experiment. A simulation was also performed of an FPSO in head seas where the pitch and heave were prescribed using an empirical forcing function. Regular waves were generated in the computation with relative heights of 30 meters. The pressure on the deck of the FPSO predicted by the computation compared fairly well with experiment. In general Kleefsman (2005) showed that a RANS and VOF approach to the water-impact problem can yield good results.

1.4.3 Wave Models

The purpose of the wave model is to induce a characteristic response of a floating body due to a spectrum of surface waves. There are two general approaches to this problem. One is to input a wave spectrum into the model and capture the dynamic response of the body. Another more straightforward approach is to use single harmonic regular waves of varying wave lengths and heights to characterize the dynamic response. For example, sea state 6 would be modeled by taking the mean wave length and height and implementing those

parameters in the wave model. Wave models that simulate higher sea states may also need a wind model because the wind can affect wave propagation and topside loads. Overall, the wave model is an essential component of the computational seakeeping tool.

Various techniques exist to create waves in viscous free-surface computations. Lal and Elangovan (2008) used a RANS and VOF technique to simulate the wave propagation induced by a flap type wave maker. The flap was implemented using prescribed mesh motion. The results of the computation matched wave model theory very well. This study showed that RANS and VOF can propagate waves with good accuracy.

Huang et al. (1998) performed simulations of a 2D numerical wave tank by using the RANS and SUMMAC (Stanford University modified marker-and-cell) techniques. The wave-maker was of the piston type and the motion was prescribed by a cosine function. The computational model implemented this wave-maker and showed good agreement with theory and experiment.

Park et al. (1999) used a RANS and marker-and-cell (MAC) method to simulate wave propagation. The inflow condition was established using linear second order Stokes wave theory. A comparison of the surface elevation during wave propagation was compared with first and second order Stokes wave theory. The numerical results compared well with second order Stokes theory very well.

These studies show that a computational viscous flow model can accurately predict the creation and evolution of surface waves.

1.4.4 Non-Reflecting Boundaries

The purpose of the seakeeping tool is to simulate a small piece of a larger reality meaning that the computational domain must be finite. In computations that involve surface waves a non-reflecting boundary condition is required. Many of the boundary conditions and techniques that have been developed in the literature are reviewed by Romate (1992), and will be reviewed here.

Periodic boundary conditions cannot be used in this application because waves may be diffracted around bodies in the flow field so the wave at the outflow boundary does not match the input wave amplitude and wave length. Moreover, the current VOF-based CFD

model allows for breaking waves, which do not conform to the requirements of the periodic boundary condition.

The Sommerfield condition described by Romate (1992), and Ma et al. (2001) applies well to potential flow but can also be implemented in viscous simulations. The equation below shows the Sommerfield condition where ϕ is any quantity and C is the wave celerity.

$$\frac{\partial\phi}{\partial t} + C\phi = 0$$

The main difficulty in implementing this type of boundary condition is that an accurate estimation of the wave celerity C near the outflow boundary is required to efficiently prevent wave reflections. Orlanski (1976) provided a method to calculate C based on the flow inside the field near the boundary. This type of boundary condition effectively operates as a high-pass filter.

The use of a numerical sponge layer, or beach, is a well suited technique for this application. An artificial viscosity, which is a function of space, is introduced into the momentum equation so energy is dissipated in a predetermined region. Cao et al. (1993) documents that the source term has the form $\nu_d(\bar{x})u_i$ where $\nu_d(\bar{x})$, is the artificial viscosity as a function of space and u_i is the fluid velocity. Wang et al. (2007) implements the sponge layer in this fashion for a viscous flow model.

$$\rho \frac{Du_i}{Dt} = -\nabla p + \mu \nabla^2 u_i + \nu_d(\bar{x})u_i$$

The artificial viscosity starts at zero at some given location in the domain and smoothly increases to its final value at the outflow boundary. The function $\nu_d(x, y, z)$, must be sufficiently smooth so that reflections do not occur at the start of the sponge layer. The chosen function $\nu_d(x, y, z)$ is arbitrary and various implementations found in the literature use cubic, hyperbolic tangent, and cosine functions to smoothly increase $\nu_d(\bar{x})$ along the beach. The use of this technique requires that the beach must be sufficiently long enough to efficiently dissipate all the wave energy which ultimately results in more computation time. This implies that the determination of the beach length requires an estimate of the wave

spectrum at the outlet. Since this knowledge cannot be known *a priori*, some tuning of the beach length and the magnitude of $\nu_d(\bar{x})$ can be expected. Clément (1996) found that the sponge layer functions most effectively as a low-pass filter for waves. Clément showed that a sponge layer coupled with a high-pass boundary condition is an efficient and effective solution to prevent wave reflections.

1.4.5 OpenFOAM

OpenFOAM is software designed to simulate many physical phenomena of interest in continuum mechanics, especially those pertaining to fluid flows and heat transfer. OpenFOAM consists of a wide range of solvers and libraries which are written in the C++ programming language. OpenFOAM relies heavily on finite volume numerics to solve systems of partial differential equations. The software is licensed under the GNU General Public License and the source code is freely obtainable. This provides a robust and very flexible development environment for a viscous seakeeping model.

Interface Capturing - VOF

Interface capturing is a technique where a free-surface is resolved within the domain. This is different from an interface tracking method where the grid must conform to the free-surface. The VOF method is widely used in interface capturing techniques. Ubbink (1997) tested the performance of the VOF method and developed a differencing scheme called CICSAM (Compressive Interface Capturing Scheme for Arbitrary Meshes), using OpenFOAM. One of the problems with using a volume fraction method such as VOF, is that numerical diffusion can show up at the interfaces between fluids. Ubbink performed various tests to study the change in fluid form as phases are convected in a computational domain. Ubbink showed that a proper selection of VOF differencing scheme can minimize numerical diffusion.

InterFOAM

InterFOAM is a solver in the OpenFOAM application suite which solves multiphase incompressible flows. CICSAM was used for some time with VOF in the interFOAM solver until

certain problems were encountered. Henry Weller, one of the original creators of OpenFOAM, developed a new algorithm which uses interface compression to replace CICSAM and today interFOAM uses this scheme. Rusche (2002) used interFOAM to test various cases of rising air bubbles in water. The velocity of an air bubble rising in a quiescent fluid was correlated well with experiments.

Recent developments of interFOAM applications were reported by Paterson (2008). The interFOAM solver was coupled with a 3DOF motion solver so that translational motions could be realized in a computation. Simulations of a floating 2D cylinder were performed for different cylinder weights and the submergence of the center-of-gravity was compared with theoretical values. The results of the computations matched these values very well.

1.5 Agenda

Chapter 2 will show how the governing equations and the numerical models are constructed and implemented. Chapter 3 will show different simulations to test the robustness of each component of a seakeeping model. For each case, the grids, boundary conditions and results are shown to demonstrate the validity of the model. Chapter 4 summarizes of these works and gives future recommendations.

Chapter 2

Governing Equations and Numerical Methods

2.1 Governing Equations

2.1.1 Turbulent Multiphase Flow Model

The flow fields are solved using the turbulent form of the Navier-Stokes equations. Closure for the Reynolds stress, τ_{ij} , is provided by the two equation K- ε turbulence model. The fluid phase fraction is calculated using the VOF method and indicated by a scalar γ which is limited to the range $[0, 1]$, where 0 and 1 represent air and water respectively. The interface between the water and air is assumed to be sharp so there is no-slip between the phases at the free-surface. The equations for mass continuity, momentum, and volume phase fraction are as follows:

$$\frac{\partial \rho}{\partial t} + \nabla \cdot (\rho \mathbf{u}_i) = 0,$$

$$\frac{\partial u_i}{\partial t} + u_j \frac{\partial u_i}{\partial x_j} = -\frac{1}{\rho} \frac{\partial p}{\partial x_i} + \frac{\partial}{\partial x_j} \left(\nu \frac{\partial u_i}{\partial x_j} + \tau_{ij} \right),$$

$$\frac{\partial \gamma}{\partial t} + \nabla \cdot (\gamma \mathbf{u}_i) = 0,$$

where ρ = density, ∇ is the nabla operator, u_i is the velocity vector, and γ is the volume phase fraction.

2.1.2 Sponge Layer

The sponge layer dissipates momentum from the water phase to reduce the surface wave elevation and fluid velocity. This is accomplished by adding an artificial term onto the right-hand side of the momentum equation which takes the form,

$$-\nu_d(x)\gamma\rho u_i.$$

$\nu_d(x)$ is the dissipation function, which is zero everywhere in the domain except in the sponge layer zone as shown in figure 2.1. The dissipation function smoothly goes from zero to its final chosen value of $\nu_{d,max}$. Clément (1996) used a cubic polynomial to prescribe $\nu_d(x)$, which is the chosen implementation here. The description of the function is shown below and is plotted in figure 2.1.

$$\nu_d(x) = \begin{cases} 0 & \text{if } x < x_{start} \\ a(x - x_{start})^3 + b(x - x_{start})^2 + c(x - x_{start}) & \text{if } x \geq x_{start} \end{cases}$$

$$a = 2(\nu_{d,max} - ML)/(-L^3), \quad b = -\frac{3}{2}aL, \quad c = M$$

The starting location of the sponge layer, x_{start} , and $\nu_{d,max}$ are specified at runtime which allows convenient manipulation of the parameters. M is the slope of the cubic at the start and end of the beach and is set equal to 0.01. γ is used in the dissipation term so that momentum is only dissipated from water where $\gamma = 1$.

2.1.3 K- ε Turbulence Model

The standard K- ε model is used in these computations. The equations for turbulent kinetic energy and dissipation rate are provided here for clarity. The Boussinesq eddy viscosity model is used to approximate the Reynolds stress.

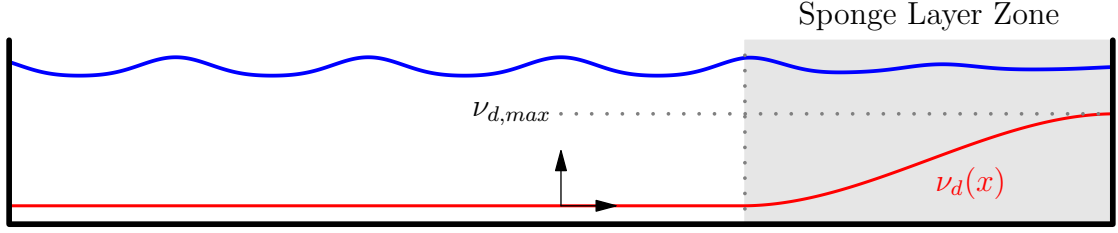


Figure 2.1: Wave Basin with sponge layer

$$\frac{DK}{Dt} = \frac{\partial K}{\partial t} + u_j \frac{\partial K}{\partial x_j} = \frac{\partial}{\partial x_j} \left(\frac{\nu_e}{\sigma_K} \frac{\partial K}{\partial x_j} \right) + \nu_e \left(\frac{\partial u_i}{\partial x_j} + \frac{\partial u_j}{\partial x_i} \right) \frac{\partial u_i}{\partial x_j} - \varepsilon$$

$$\frac{D\varepsilon}{Dt} = \frac{\partial \varepsilon}{\partial t} + u_j \frac{\partial \varepsilon}{\partial x_j} = \frac{\partial}{\partial x_j} \left(\frac{\nu_e}{\sigma_\varepsilon} \frac{\partial \varepsilon}{\partial x_j} \right) + \frac{C_{\varepsilon_1} \nu_e \varepsilon}{K} \left(\frac{\partial u_i}{\partial x_j} + \frac{\partial u_j}{\partial x_i} \right) \frac{\partial u_i}{\partial x_j} - C_{\varepsilon_2} \frac{\varepsilon^2}{K}$$

$$\sigma_K = 1.0 \quad \sigma_\varepsilon = 1.3 \quad C_\mu = 0.09 \quad C_{\varepsilon_1} = 1.44 \quad C_{\varepsilon_2} = 1.92$$

$$\nu_e = C_\mu \frac{K^2}{\varepsilon}$$

$$E_{ij} \equiv 1/2 \left(\frac{\partial u_i}{\partial x_j} + \frac{\partial u_j}{\partial x_i} \right)$$

$$\tau_{ij} = -\overline{u_i u_j} \approx -\frac{2}{3} K \delta_{ij} + 2\nu_e E_{ij}$$

2.1.4 6 Degree-of-Freedom Equations

Translational Motion

Newton's second law of motion is used to describe the translational motion of bodies. This gives 3 equations of motion in the x , y , and z directions.

$$F_i = ma_i$$

The force is calculated by integrating the pressure and shear stress over the surface of the body. This is done by taking the sum of the forces, $F_{i,\text{pressure}}$ and $F_{i,\text{viscous}}$, due to

pressure and viscous effects for every cell face on the body boundary. Figure 2.2 shows how the cell faces are defined for a body boundary. The body-fixed axes are also shown in this figure. The equations for the forces due to pressure and viscous effects are as follows,

$$F_{i,\text{pressure}} = \sum_{\partial B} p A_i n_i,$$

$$F_{i,\text{viscous}} = \sum_{\partial B} -\nu_f \frac{\partial u_i}{\partial n_i} A_i,$$

$$F_i = F_{i,\text{pressure}} + F_{i,\text{viscous}},$$

where p is the pressure in a given cell, A_i is the magnitude of area on a cell face, n_i is the normal vector on the cell face, and ν_f is the viscosity in the cell.

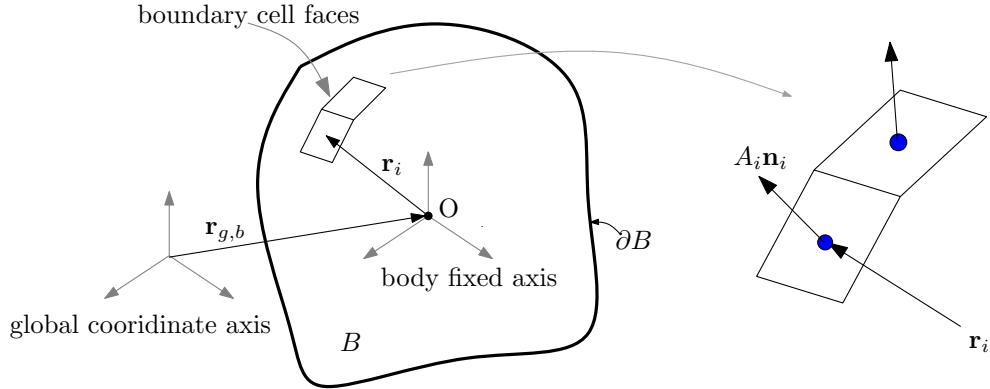


Figure 2.2: Body boundary

The translation velocity u_t is then calculated using a fifth-order Cash-Karp embedded Runge-Kutta solver shown by Press et al. (1992).

Rotational Motion

Euler's equations of motion are used to describe the rotational motion.

$$M_O = \left(\dot{H}_O \right)_{xyz} + \omega \times H_O$$

Where H_O is defined as the angular momentum:

$$H_O = I\omega.$$

Since the axes are fixed to the body, the inertia tensor I will have the form,

$$I = \begin{pmatrix} I_x & 0 & 0 \\ 0 & I_y & 0 \\ 0 & 0 & I_z \end{pmatrix}$$

M_O is calculated by summing the moments about the center of gravity (CG) over the body due to the pressure and viscous forces and moments.

$$M_O = M_{i,\text{pressure}} + M_{i,\text{viscous}}$$

$$M_{i,\text{pressure}} = \sum r_i \times F_{i,\text{pressure}}$$

$$M_{i,\text{viscous}} = \sum r_i \times F_{i,\text{viscous}}$$

The angular velocity ω_r about the CG is calculated using a fifth-order Cash-Karp embedded Runge-Kutta solver (Press et al., 1992). The translation velocity $u_{r,i}$ due to rotational motion for each boundary cell face, indicated by an index i , is then calculated .

$$u_{r,i} = \omega_r \times r_i$$

6DOF Model Realisation

The velocity of each boundary cell face, due to both the translational and rotational motion, is then calculated.

$$u_{\text{boundary},i} = u_t + u_{r,i}$$

This velocity is then inputted into the mesh motion solver, which moves the boundary and updates the mesh. Figure 2.3 shows how the motions are imposed by the translational and rotational components of velocity.

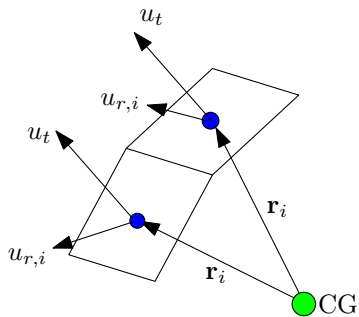


Figure 2.3: Boundary cell face velocity vectors

2.1.5 Surface Wave Models

Two wave models for deep and shallow water waves are developed and shown in these sections. In general the wave models are derived from linear theory and the wave surface follows a 2nd order Stokes wave.

2nd-order Stokes Wave

A 2nd-order Stokes approximation is chosen to predict the sharper crests and flatter troughs observed in actual surface waves. In most practical applications, a 2nd order Stokes wave is satisfactory (Beck et al., 1989). $\eta(x, t)$ is the wave elevation function used for both shallow and deep water waves. See figure 2.1 for a representation of a 2nd order Stokes surface wave.

$$\eta(x, t) = A \cos(kx - \omega_w t) + \frac{1}{2} k A^2 \cos 2(kx - \omega_w t)$$

Shallow Water

In very shallow water, where $h < \frac{\lambda}{25}$, the wave celerity can be approximated as

$$V_c^2 = gh.$$

This yields the following equations for the components of velocity in water after plugging V_c into the potential. Here u and v are the fluid velocity

$$u = \frac{gAk}{\omega_w} \frac{\cosh k(y+H)}{\cosh kh} \cos(kx - \omega_w t)$$

$$v = \frac{gAk}{\omega_w} \frac{\sinh k(y+H)}{\cosh kh} \sin(kx - \omega_w t).$$

Deep Water

In deep water, where $h > \frac{\lambda}{2}$, the wave celerity can be approximated as

$$V_c^2 = \frac{g}{k} = \frac{g\lambda}{2\pi}.$$

This gives the following equations for the velocities:

$$u = A\omega_w e^{ky} \cos(kx - \omega_w t)$$

$$v = A\omega_w e^{ky} \sin(kx - \omega_w t).$$

2.2 Numerical Methods

2.2.1 General Method of Solution of Multiphase Solver

The simulation takes the following steps each time step:

1. Adjust time step according to Courant number
2. Mesh motion equation solved if dynamic mesh is implemented
3. γ equation solved with explicit MULES technique
4. Momentum equation solved
5. Pressure field solved with PISO technique
6. Solve turbulence equations (K- ε) and correct turbulent viscosity

2.2.2 Boundary Conditions

Wave Maker Boundary Condition

The wave maker boundary condition specifies γ and fluid velocity on a boundary. The second-order Stokes equation for $\eta(x = 0, t)$ is used to calculate γ at the boundary. The selection for either shallow or deep water wave model is specified at runtime. Each model specifies the components of the inlet velocity u_i on the cell boundary faces. Figure 2.4 shows how the wave maker boundary condition works on a boundary face. The dots represent the face centers, $y_{\text{centered},i}$, and are colored by phase (red = water, blue = air). If $y_{\text{centered},i} \leq \eta(t)$, then the inlet phase is chosen as water and the velocities, u_i , are calculated for each $y_{\text{centered},i}$. The sea level depth, H , which is used by the shallow water wave model, and gravity direction, g , are indicated in figure 2.4.

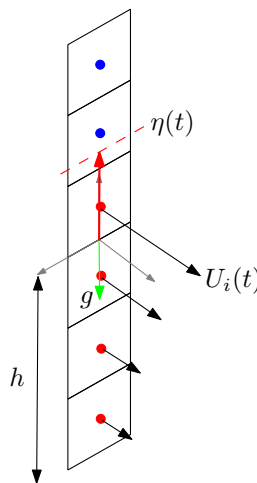


Figure 2.4: Wave boundary condition realisation

Built-in OpenFOAM Boundary Conditions

OpenFOAM has several boundary conditions built-in, which are used throughout the computations. Table 2.1 summarizes a selection of boundary conditions.

Type	Description
Zero Gradient	Normal gradients are set to zero
Fixed Value	Values are specified
No Slip	Fixed Value of (0, 0, 0)
Moving Wall Fixed Value	Values are specified and set relative to patch velocity
Moving Wall No Slip	Fixed value of (0, 0, 0) set relative to patch velocity
Slip	Normal component has a fixed value of zero and tangential components are specified with zero gradient
Total Pressure	Calculated as $p = p_0 - \frac{1}{2}\rho \mathbf{U} ^2$, where p_0 is specified at runtime
Advective	$\frac{D}{Dt}(\phi) = \frac{\partial\phi}{\partial t} + C\phi = 0$, where C is calculated at the boundary
Oscillating Fixed Value	$\phi = A \cos(2\pi ft)$
Inlet Outlet	Switches value between two values based on direction of velocity
Pressure Inlet Velocity	When p is known, calculate U from flux
Pressure I/O Velocity	Combination of Pressure Inlet Velocity and Inlet Outlet

Table 2.1: OpenFOAM boundary conditions

2.2.3 Finite Volume Method

The finite-volume method is a technique for evaluating partial differential equations. OpenFOAM implements a cell-centered FVM. Each mesh cell has boundary faces, a center value, and a volume. The flux through a cell volume is conserved. All the equations for fluid flow are discretized using first and second order schemes.

2.2.4 Mesh Motion

The mesh motion is accomplished by diffusing the velocity of points via a Laplace equation of the form,

$$\nabla \cdot (k \nabla u_{i,\text{mesh}}) = 0,$$

where k is a distance function whose purpose is to minimize the mesh distortion, and $u_{i,\text{mesh}}$ is the velocity of points in the mesh. k is chosen as an inverse quadratic of the form, $k = 1/l^2$, where l is the distance to the moving boundary. The mesh motion equation is solved using the finite element method to diffuse the motion of a boundary to other points in the domain. The main reason to choose FEM over FVM is that interpolation from cell-centers to vertices is not required.

Chapter 3

Computations

This chapter presents the simulations that are performed to verify each component of the overall seakeeping model. For each case, the grid, simulation parameters, and analysis is presented. First, a simple case with prescribed motion and single phase flow is presented to validate the Navier-Stokes flow model and the mesh motion technique. A practical example of prescribed mesh motion with the free-surface model is then presented. The major components of the seakeeping model (6DOF, mesh motion, free-surface VOF, turbulent viscous hydrodynamics, and shallow-water wave model) are then validated using free-decay and wave-excited numerical experiments of a 2D box barge. Studies are then presented to validate the deep-water wave model. The effectiveness of the sponge layer as a function of the dissipation and beach length parameters is then presented. Wave-slap load simulations are performed to study scaling effects and grid dependency. A practical example of a numerical wave-slap experiment is then presented. Together these sections demonstrate the robustness and validity of each component of the seakeeping model.

3.1 Prescribed Body Motion and Laminar Single-Phase Navier-Stokes Fluid Model

3.1.1 Oscillating Cylinder

Nobari and Naderan (2006) studied the loads on a 2D cylinder which is prescribed to oscillate transversely and inline with the uniform flow direction. Vortices are shed off the cylinder at a Reynolds number of 100. This induces a load on the cylinder and the lift coefficient is computed over time. This allows an FFT to be performed to correlate the vortex shedding frequency with the prescribed oscillation frequency. A phenomena known as lock-on can occur when vortices are shed at the same frequency at which the cylinder is oscillating. The paper looked at different amplitudes and frequencies of oscillation to determine where the lock-on range existed and compared the results with the theoretical range. The cylinder displacement, $y(t)$, was prescribed with a sine function as $y(t) = Y \sin(2\pi ft)$. A similar computation is performed here to verify that the RANS model works with prescribed mesh motion. Figure 3.1b shows how the cylinder oscillates with respect to the in flow U . The mesh quality is also examined as the mesh is deformed during cylinder oscillation.

Grid

The grid as shown in figure 3.1 was generated with 32610 cells. It is a hybrid mesh containing both structured and unstructured cells.

Boundary Conditions

Conditions for inlet velocity and outlet pressure are set for the simulation according to table 3.1.

Boundary	Pressure	Velocity	Mesh Velocity
Cylinder Wall	Zero Gradient	Moving Wall No Slip	Oscillating Fixed Value
Left	Zero Gradient	Fixed Value	Slip
Right	Total Pressure	Zero Gradient	Slip
Top	Zero Gradient	Slip	Slip
Bottom	Zero Gradient	Slip	Slip

Table 3.1: Boundary conditions

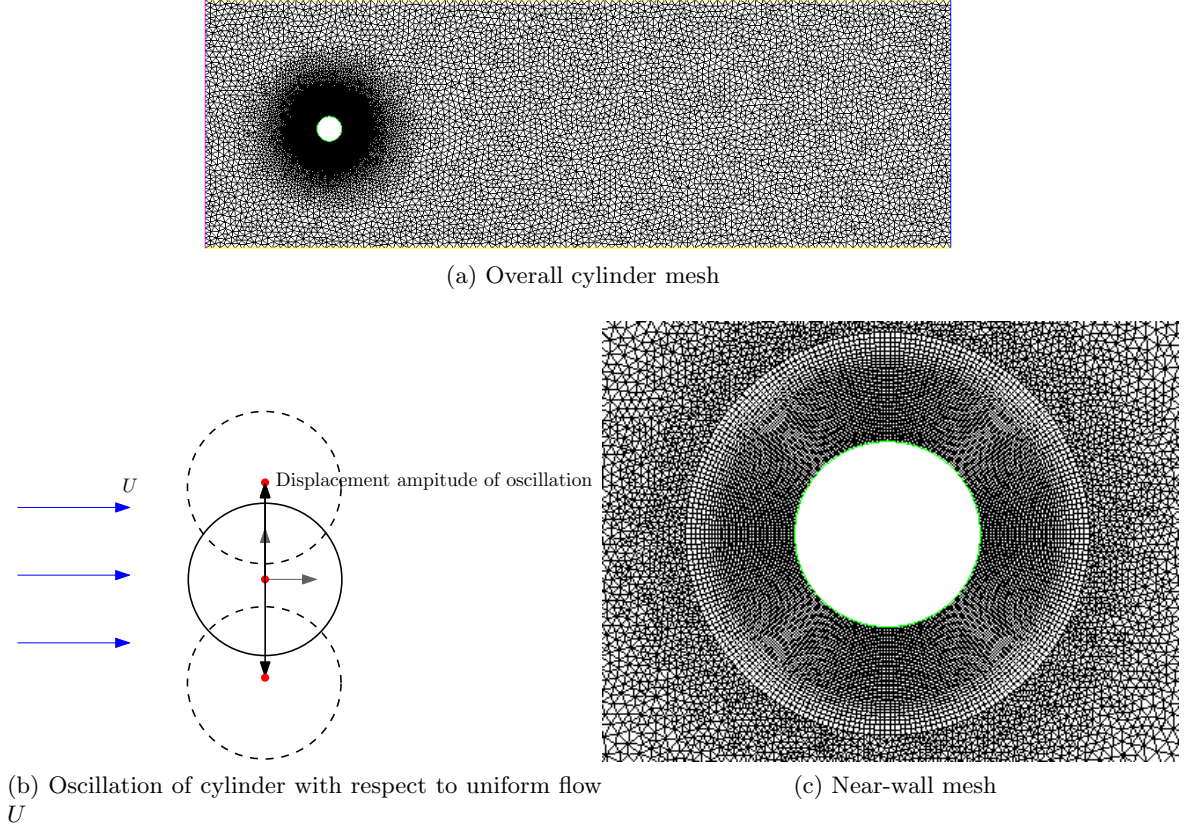


Figure 3.1: Cylinder mesh and prescribed motion description

The parameters for the oscillation frequency in this simulation are then set to the same values used by Nobari and Naderan (2006). Two cases are selected for which the FFT plots were presented in the aforementioned paper. The following definitions for displacement amplitude Y and frequency f are shown below. The displacement Y is normalized by the cylinder diameter d and frequency f is normalized by the Strouhal frequency f_s . The Strouhal number for the case of a cylinder is taken to be 0.18.

$$A = \frac{Y}{d}, \quad F = \frac{f}{f_s}, \quad St = \frac{f_v d}{U} = 0.18$$

Nobari and Naderan (2006) defined the cylinder motion by prescribing the position of cylinder. In the current simulation the velocity of the cylinder is prescribed. Therefore, the motion velocity oscillation amplitude and frequency are defined as,

$$a = 2\pi f Y d, \quad f = F f_s,$$

where the velocity of the cylinder is prescribed as $u_{cylinder}(t) = a \cos(2\pi ft)$. The cases are then run with the parameters shown in table 3.2.

Case Designation	A	F
1	0.2	0.6
2	0.2	1.05

Table 3.2: Cylinder test cases

Analysis

The flow fields are analyzed to verify vortices are being shed and that the results in general meet expectations. Figure 3.2 shows the cylinder oscillating through approximately one period and shedding a vortex. The color scale shows positive and negative vorticity to indicate the rotation direction of vortices.

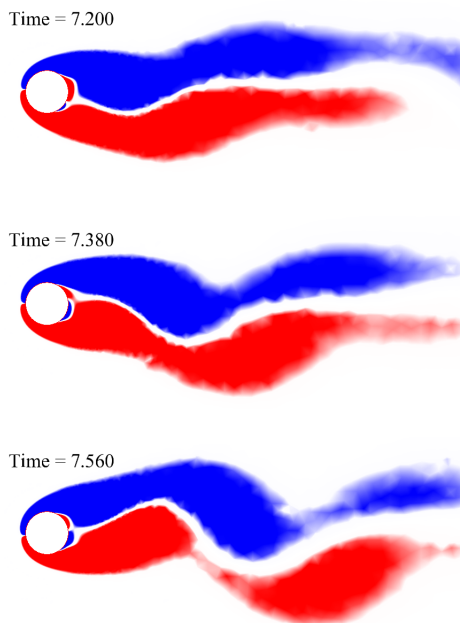


Figure 3.2: Vortex shedding, $A = 0.2$, $F = 1.05$, $Re = 100$, red = positive vorticity, blue = negative vorticity

The times are non-dimensionalized in the form, $t^* = tU/d$. An FFT of the lift coefficient data is then taken and correlated with the analysis done by Nobari and Naderan (2006). The results of case 1 in figure 3.3 demonstrate that vortex lock-on does not occur when $A = 0.2$ and $F = 0.6$ because a second peak shows up near a non-dimensional frequency of

0.1. This secondary peak seen in case 1 matches well with the second peak seen in Nobari's study. The dominant peaks in both cases are close to the Strouhal number of 0.18 which is further confirmation of the results. Case 2 shows that when the prescribed oscillation frequency is close to the Strouhal frequency lock-on occurs, as shown in figure 3.3 where only one peak is present. The results agree well with the computation done by Nobari and Naderan (2006) and the experimental Strouhal number for a cylinder.

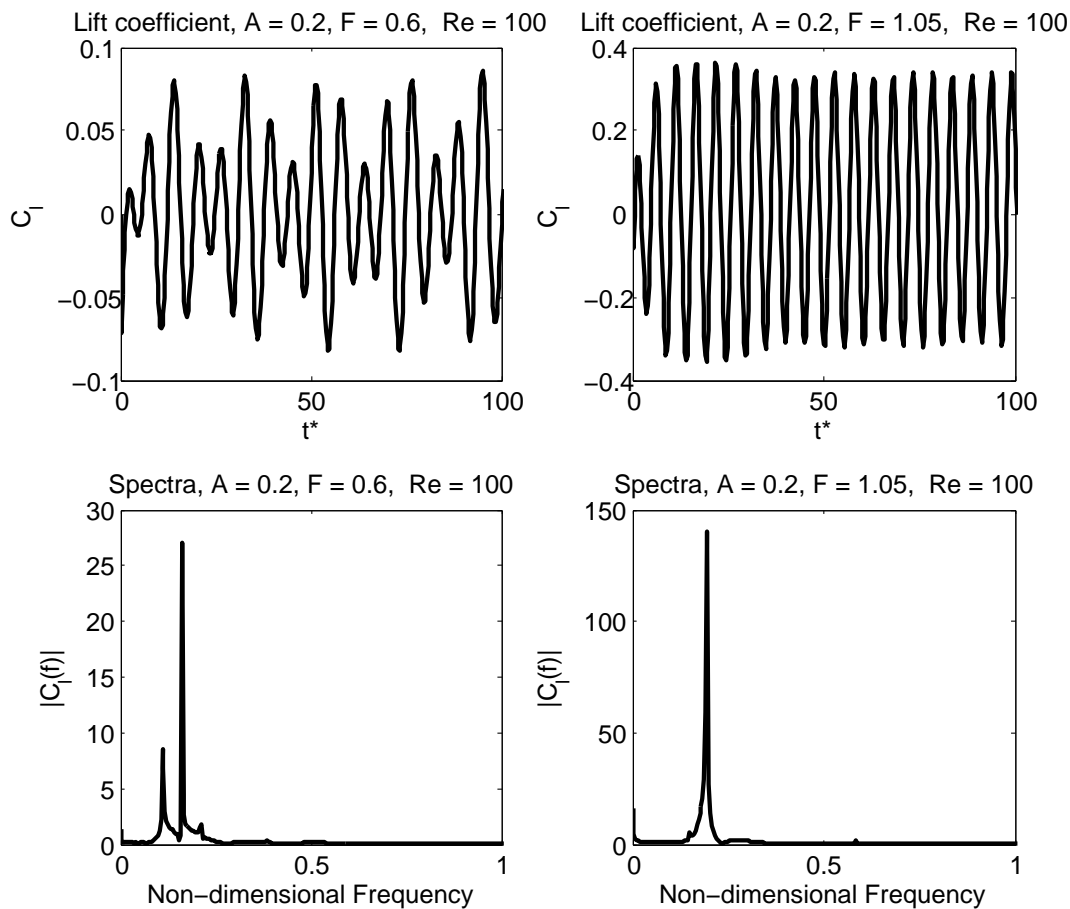


Figure 3.3: Oscillating cylinder results - Case 1: $A = 0.2$, $F = 0.6$ - Case 2: $A = 0.2$, $F = 1.05$

The mesh at the moment of maximum deformation is shown in figure 3.4. In general the mesh quality looks good given the relatively small amplitude motion and simple geometry.

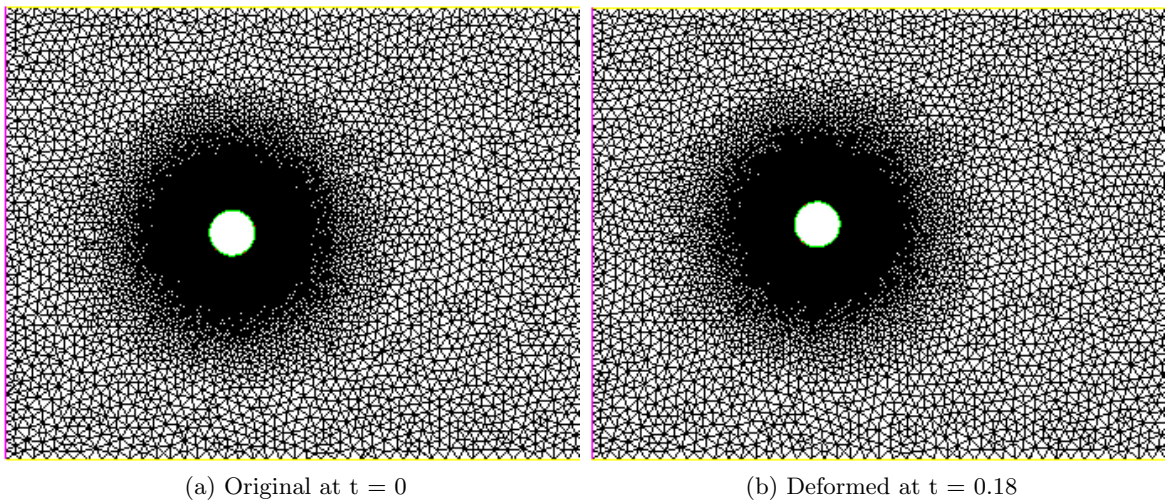


Figure 3.4: Deformed cylinder mesh

3.2 Prescribed Body Motion and Free-Surface RANS

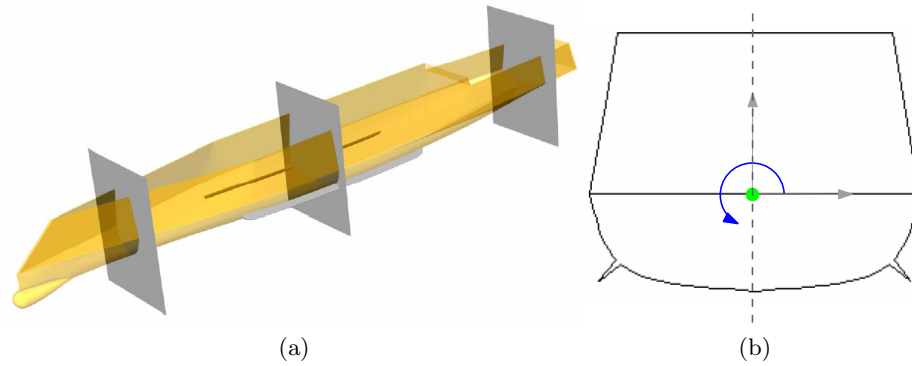
3.2.1 Prescribed Roll Oscillation of Tumblehome Midship Geometry

This section shows how prescribed motion can be applied to free-surface problems with reasonably complex geometries. An ONR Tumblehome (ONRTH) midship 2D section was prescribed to roll about an axis. Figure 3.5 shows what the full 3D geometry looks like as well as different sections of the hull. Simulations for the midship section with and without bilge keels are performed and the results are compared. The roll amplitude and frequency sets, $\{a\} = \{5^\circ, 15^\circ, 30^\circ\}$ and $\{f\} = \{2.17 \text{ rad/s}, 3.81 \text{ rad/s}, 4.83 \text{ rad/s}\}$, are used to form a matrix of test cases.

Grids

Barehull Figure 3.6 shows the bare hull mesh that was in the computations. The grid is fully structured and is composed of 25258 cells.

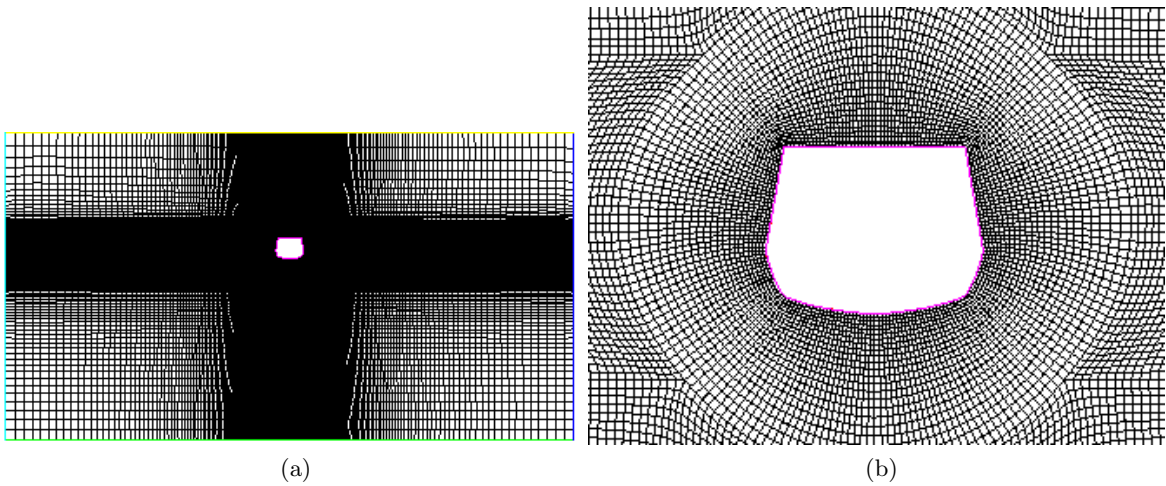
Bilgekeels This mesh has a higher fidelity to capture the flow around the bilgekeels and contains 51148 structured cells. The bilgekeels mesh is shown in figure 3.7.



(a)

(b)

Figure 3.5: ONRTH sections



(a)

(b)

Figure 3.6: ONRTH bare hull mesh

Flow Boundary Conditions

Table 3.3 shows the flow boundary conditions that were used in the computations.

Roll Motion

The roll motion of the hull is prescribed by specifying the angular displacement about the specified axis shown in figure 3.5b. The roll angle over time is defined as

$$\theta = a \sin(2\pi ft)$$

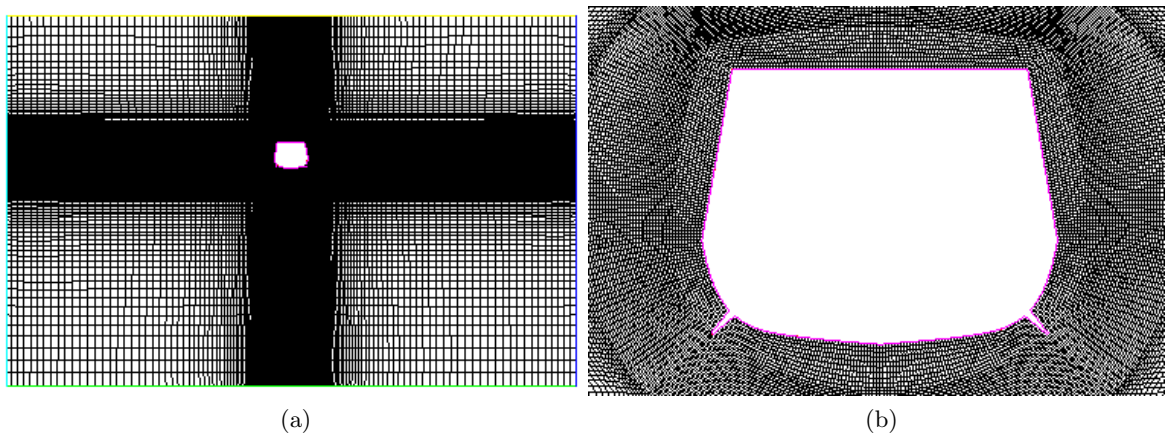


Figure 3.7: ONRTH bilgekeels mesh

Boundary	Pressure	Velocity	Gamma	Mesh motion
Midship Section	Zero Gradient	Moving Wall Fixed Value	Zero Gradient	Prescribed
Left	Zero Gradient	Fixed Value (0, 0, 0)	Zero Gradient	Slip
Right	Total Pressure	Fixed Value (0, 0, 0)	Zero Gradient	Slip
Top	Zero Gradient	ZeroGradient	Inlet Outlet	Slip
Bottom	Zero Gradient	Slip	Zero Gradient	Slip

Table 3.3: ONRTH midship boundary conditions

for each case. At each time-step the rotation amplitude is calculated and imposed on the hull. The mesh motion solver then calculates the new positions of all other points in the domain.

Analysis

The flow field of a selected bilge keels case is analyzed. Figure 3.8 shows how vortices are shed from the bilge keels. There are some oscillations or capillary waves at the surface near the hull, but experimental data is needed to confirm or refute this aspect of the flow solution. This phenomena is seen in other computations and may be a numerical artifact due to the mesh motion. The barehull geometry does not shed vortices in water and therefore will not provide nearly as much roll damping as the geometry with bilgekeels. The deformed bilge keels mesh is shown in figure 3.9. This is the case with a roll amplitude of 30° . The mesh quality has decreased, but given the relatively high amplitude motion and complex geometry this mesh motion method proves to be quite robust.

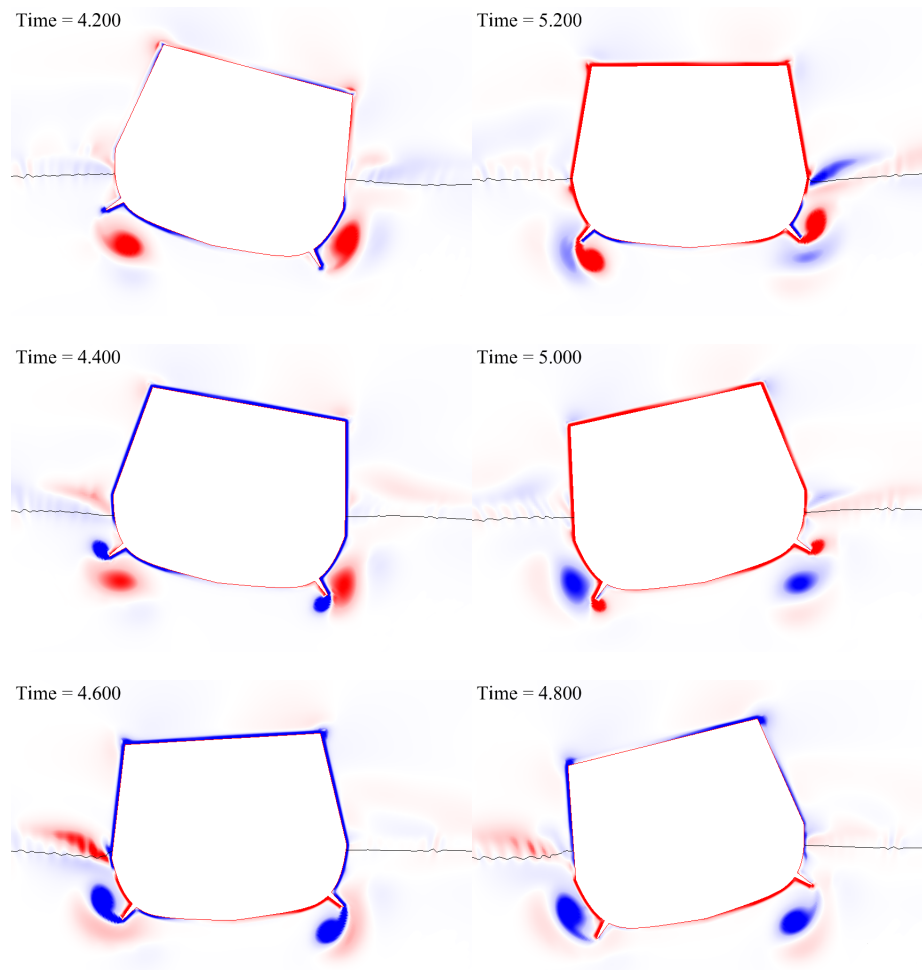


Figure 3.8: Bilge keels vortex shedding, $A = 15^\circ$, $F = 4.83$ rad/s. Red = positive vorticity, Blue = negative vorticity, Black line indicates free-surface

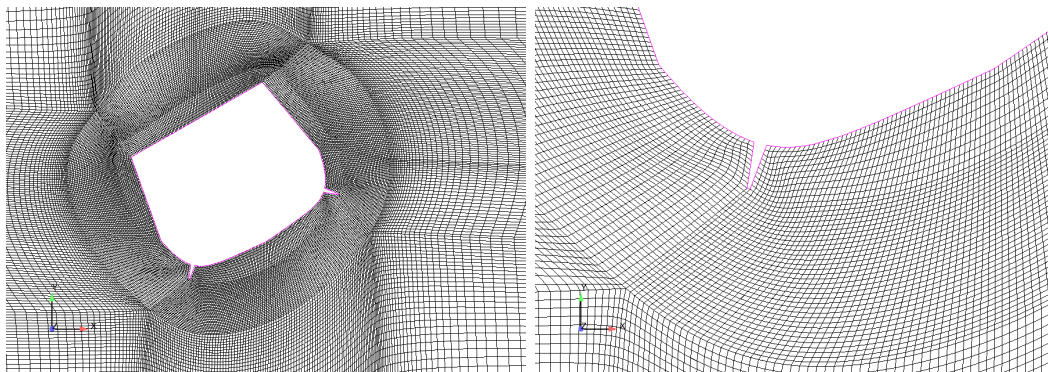


Figure 3.9: ONRTH bilgekeels mesh deformed. Amplitude = 30° , Frequency = 4.83 rad/s

3.3 Free Rigid-Body Motion and Free-Surface RANS

3.3.1 Free-Roll of 2D Box Barge

A free-roll simulation of a 2D box barge is compared with an experiment performed by Jung et al. (2006). This simulation allows 1 DOF for roll about an axis. The barge is initially inclined to 15° and is then allowed to free-roll about an axis as indicated in figure 3.10. No translation of barge is permitted per the experimental setup. The decay of roll is analyzed and the natural frequency of roll is compared with experiment.

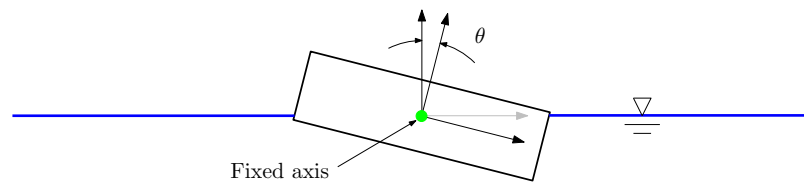


Figure 3.10: 2D box barge free-roll problem schematic

Grid

The mesh was generated to a relatively high fidelity to capture any flow separation that could affect the roll damping of the barge. Sarkar and Vassalos (2000) showed that sharp corners of cylindrical bodies can affect the hydrodynamic coefficients of roll obtained by computations. Their solution was to add a small bilge radius which was 0.625% of the beam length. Grids with and without a bilge radius are generated to illustrate this phenomena. Figure 3.11 shows the various zoom levels of the bilge radius grid for clarity. The mesh is then deformed to give the initial angle of inclination. The deformed mesh is shown in figure 3.11d.

Flow Boundary Conditions

This simulation uses the same boundary conditions on pressure, velocity, and gamma as the ONRTH prescribed roll motion case. This is shown in table 3.3 for reference.

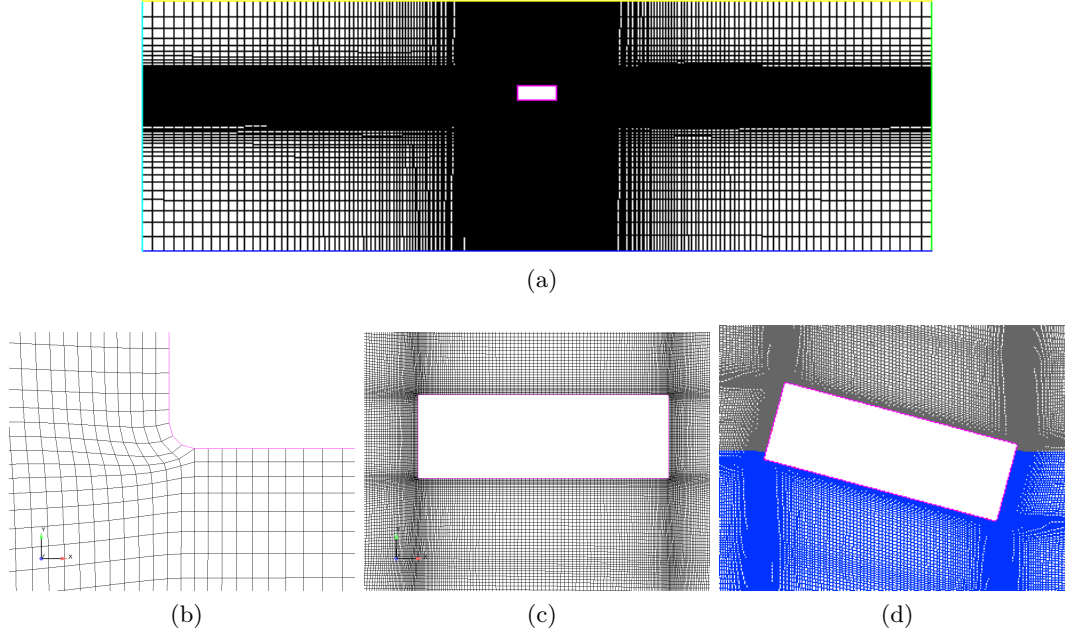


Figure 3.11: 2D barge with bilge radius. (d) Initial conditions, 15° of inclination, Blue indicates water

Analysis

For a free-roll decay test the equivalent linear equation of motion is in the form,

$$\frac{d^2\phi}{dt^2} + 2\zeta\omega_N \frac{d\phi}{dt} + \omega_N^2\phi = 0,$$

where ζ is the damping factor and ω_N is the natural frequency of roll (Jung et al., 2006). The damping factor is computed as $2\zeta\omega_N = b/I'$, where b is the damping coefficient and I' is the virtual mass moment of inertia. The formulation of b is given from Bhattacharyya (1978) as,

$$b = \frac{K_1 T_\phi \Delta G M_T}{\pi^2}.$$

Values for K_1 and T_ϕ are obtained using a curve-of-extinction which is a technique described by Bhattacharyya (1978). The damping factor ζ is computed from b , the experimental value of I' , and the numerically found ω_N . This value is then compared against the experimental result.

The natural frequency in both cases is approximately the same and matches well with

experiment. This can be expected because the moment of inertia is set to the same value for both cases and there is negligible change in geometry due to adding the bilge radius. The effect of adding a small bilge radius only affected the damping factor ζ . Table 3.4 shows a summary of the results. It is interesting to see that the coarser mesh with no bilge radius yields a more accurate damping factor. This is most likely due to the fact that the experimental setup introduced some frictional damping at the fixed axis of the barge. The assumption of 2D flow was also made in these computations which could be part of the error.

Case	ω_N rad/s	Error	ζ	Error
CFD 0.625% BR	6.90	1.8%	0.0877	17.3 %
CFD No BR	6.90	1.8%	0.0980	7.54 %
EFD	6.78	-	0.106	-

Table 3.4: Free decay results comparison

3.3.2 Wave-induced Roll of 2D Box Barge

Jung et al. (2006) also performed experiments which characterized the roll response of the box barge in waves. These simulations limit the motion to allow 1DOF for roll about an axis and are assumed to be 2D. Figure 3.13 shows a schematic of the simulation with the wave maker at one end and the barge fixed at an axis indicated by the green dot.

Grid

The grid for these simulations was adapted from the previous free-roll case with a bilge-radius. The grid between the wave-maker and the barge was constructed to a high resolution to capture the waves correctly. During the gridding and testing process it was noticed that stretched cells tended to dissipate energy from waves. Therefore the cells are stretched after the barge to save computation time and dissipate as much wave energy as possible so any reflections do not affect the solution considerably. The region between the wave maker and the box barge consists of uniformly spaced cells along the direction of wave propagation. Figure 3.14 shows the overall grid and a close up view of the wave propagation region with uniform cell spacing.

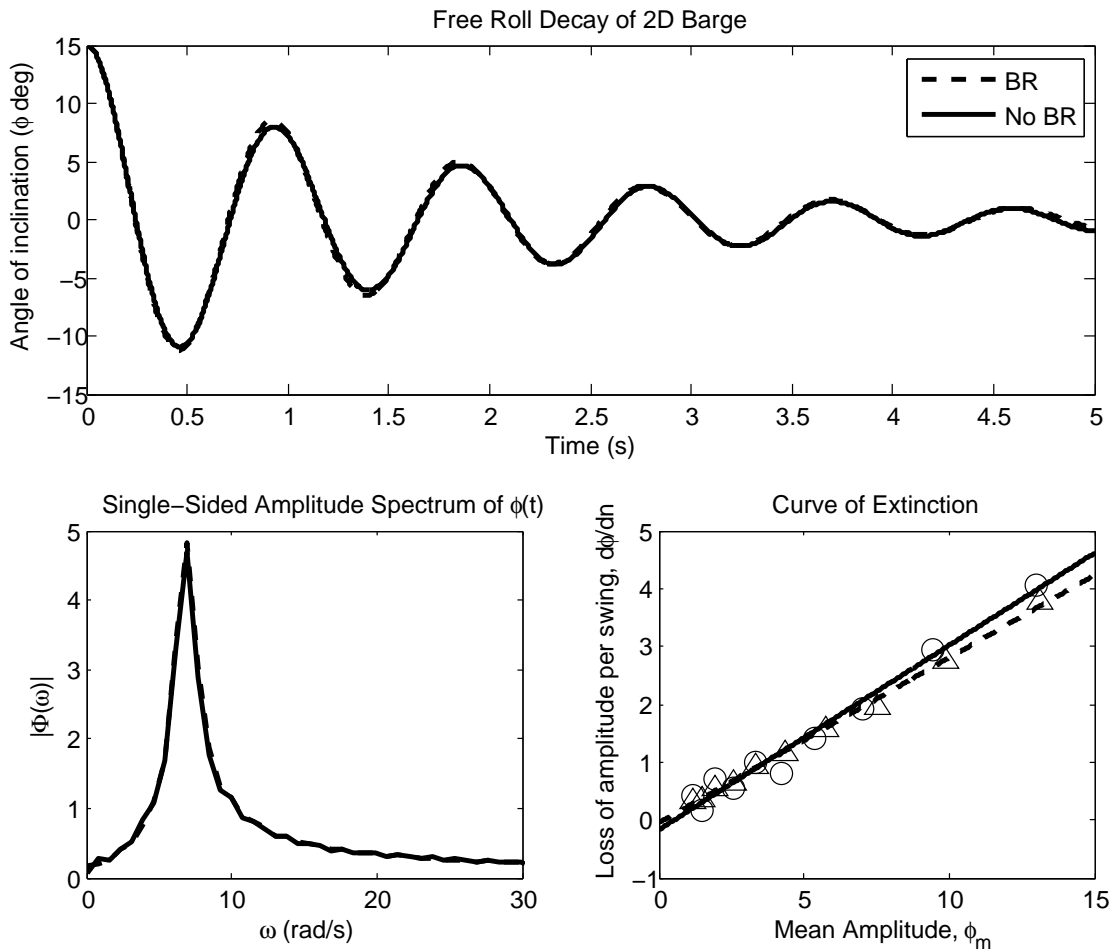


Figure 3.12: Free roll decay analysis. Solid line = 0.625% bilge radius case. Dashed line = No BR case.

Boundary Conditions

The boundary conditions for this case are shown in table 3.5.

Wave Parameters

Wave parameters were selected so that the resulting magnification factors could be compared with the EFD results obtained by Jung et al. (2006). The simulation parameters in table 3.6 were varied and run automatically using scripting techniques in Linux.

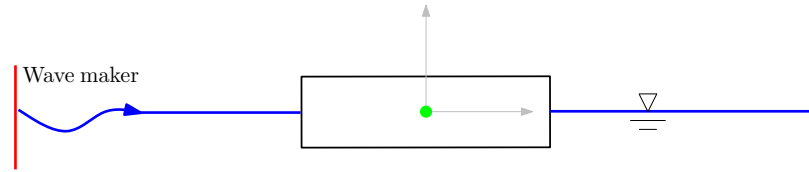


Figure 3.13: 2D box barge wave-excited roll problem schematic

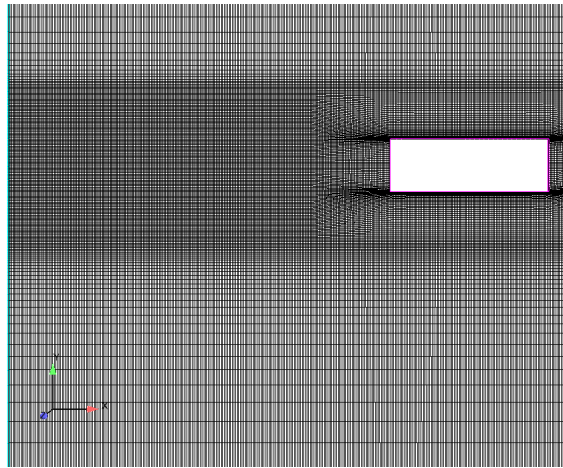


Figure 3.14: 2D barge grid with high fidelity for wave propagation

Analysis

The magnification factor ϕ/kA is taken as the result of each case where ϕ is the maximum angle-of-inclination seen during the simulation. ϕ is normalized by the incoming wave steepness kA . Figure 3.15 shows the results plotted against the experimental magnification factors. The x-axis in figure 3.15 is the radial frequency of the incoming wave ω normalized by the natural frequency of the barge ω_N . This figure shows that the computational model results compares well with experiment. At $\omega/\omega_N = 1$ the resonance peak is observed. It is interesting to note that at frequencies above the natural frequency more damping occurs whereas below the natural frequency less damping occurs. In general the computational results agree well with the experiment.

Boundary	Pressure	Velocity	Gamma	Mesh motion
Midship Section	Zero Gradient	Moving Wall No Slip	Zero Gradient	1DOF
Left	Zero Gradient	Shallow Water Wave	2nd Order Stokes	No Slip
Right	Total Pressure	Zero Gradient	Zero Gradient	No Slip
Top	Zero Gradient	Zero Gradient	Inlet Outlet	No Slip
Bottom	Zero Gradient	Slip	Zero Gradient	No Slip

Table 3.5: Boundary conditions for wave-induced box barge cases

λ [m]	0.56	0.77	1.00	1.13	1.35	1.56	1.88	2.22	2.57	3.29
H [m]	0.017	0.015	0.029	0.033	0.016	0.044	0.057	0.032	0.060	0.062

Table 3.6: Wave parameters

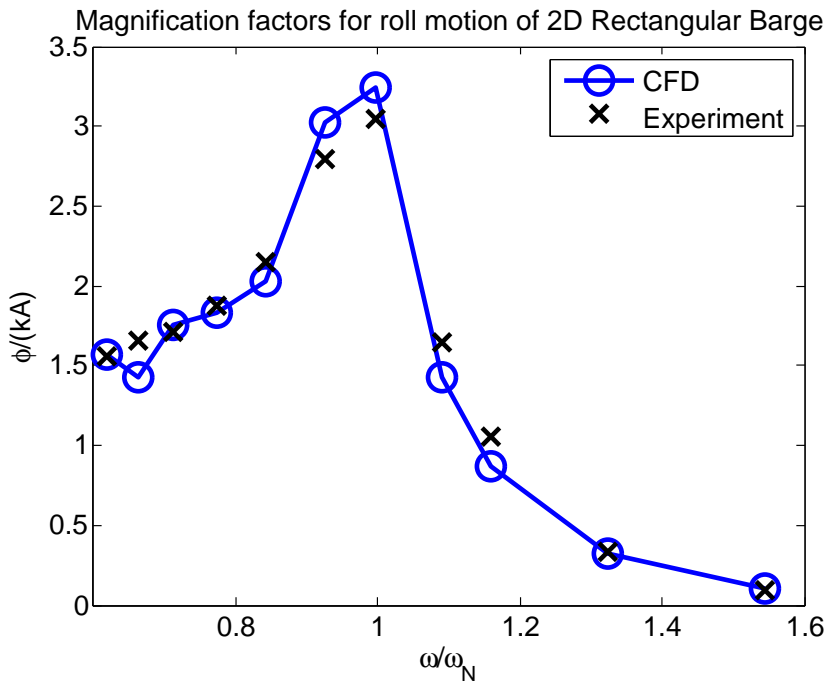


Figure 3.15: Magnification factors

3.4 Deep Water Wave Model

3.4.1 Dependency on Basin Depth

This study is performed to look at the effect of basin depth on the wave propagation form of large amplitude deep water waves. Various basin depths are selected and the results are compared against each other to check for inconsistencies. The grids have depths of 25, 50, and 100 meters. Regular waves are generated with wave heights representative of sea states 5 and 6 in these computations to look for any dependency of wave propagation on grid depth.

Grids

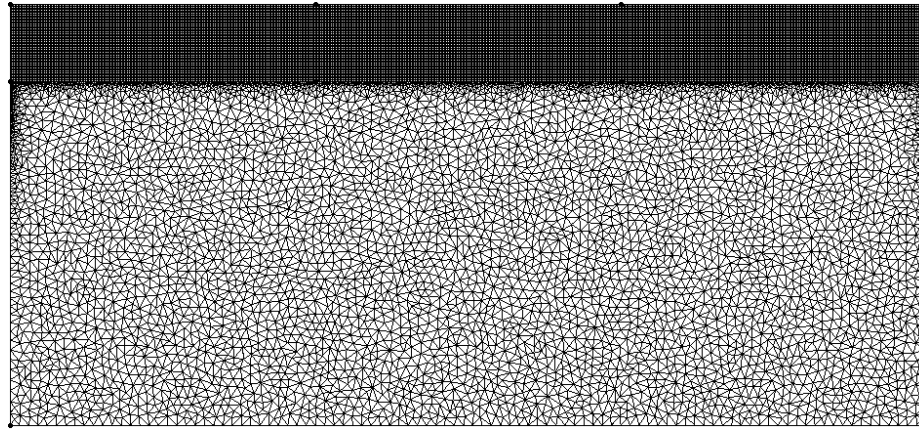
The grids used in these simulations are hybrid meshes consisting of structured and unstructured cells. A relatively fine structured mesh contains the region where the wave surface is propagating and an unstructured mesh in the region below the wave surface. There are low gradients of velocity and pressure below the surface so a relatively coarse unstructured mesh is sufficient. Grid B is shown in figure 3.16a. The 3 grid depths selected for this study are shown in table 3.16b.

Wave Parameters

Sea states 5 and 6 are selected for these simulations. Mean wave heights for each sea state are taken from the data presented by Beck et al. (1989). The wave steepness, $X = H/\lambda$, is set to 0.05 and the wave length λ is calculated. These parameters are shown in table 3.7

Sea State	H [m]	λ [m]	Steepness X
5	3.25	65	0.05
6	5	100	0.05

Table 3.7: Deep water wave parameters



(a) Grid B, 50 meter basin depth

Grid	Basin depth [m]	Number of cells
A	100	36817
B	50	40451
C	25	37903

(b) Meshes

Figure 3.16: Deep-water wave grids

Analysis

The results of each case are shown in figure 3.17. The wave surface is shown at $t = 20$ seconds for all cases. Sea state 5 is slightly affected by the grid depth in these cases as shown by the results from Grid C. The results for sea state 6 show that grid depth can drastically change the wave propagation and surface elevation. These results meet the expectation that when the condition $h > \frac{\lambda}{2}$ is not satisfied the wave propagation will be affected by the depth.

3.4.2 Wave Breaking Limit

Melville (1982) studied the breaking and instability of deep water waves as the steepness, $X = H/\lambda$, is varied. The experiment concluded that a steepness of $X > 0.05$ results in a breaking wave. One of the major advantages of using a non-linear flow model is that wave breaking can be captured and predicted. The current study will compare computational results with the experimentally observed breaking limit. At the same time the robustness of the model will be tested using high amplitude sea states with varying degrees of steepness. The expected type of breaking waves are known as spilling breakers. An example of a

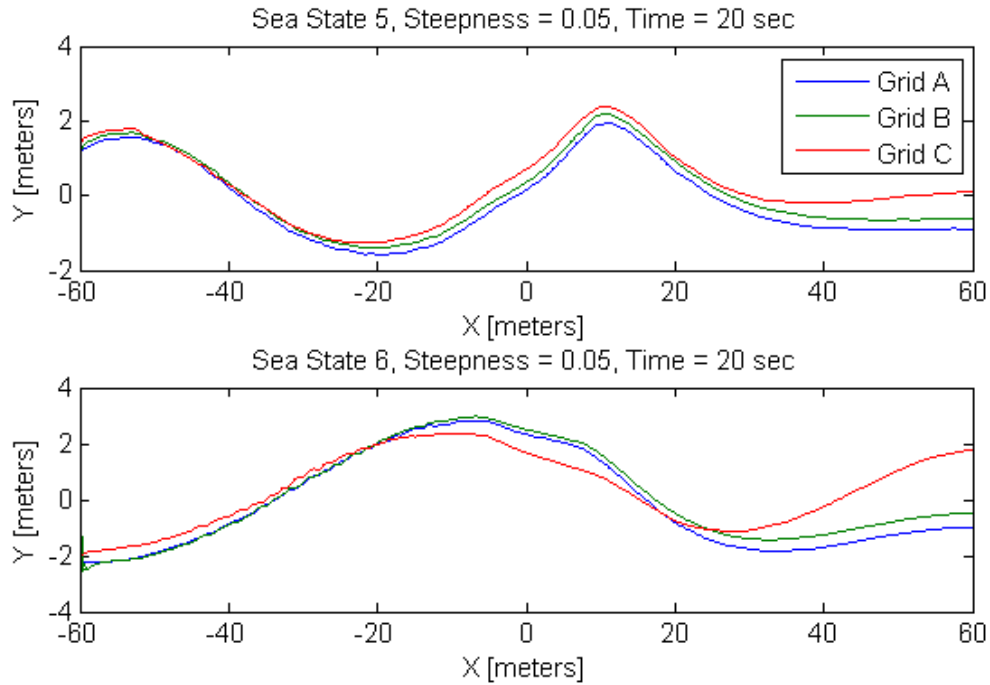


Figure 3.17: Deep water wave propagation dependency

spilling breaker evolution is shown in figure 3.18.

Grid

The grid used in these computations is grid B from the previous computation with a depth of 50 meters.

Wave Parameters

Sea state 5 is set as the wave height across this set of simulations and the steepness is varied above and below the experimental wave breaking limit. The wave steepness set under consideration is $\{X\} = \{0.03, 0.04, 0.05, 0.06, 0.07, 0.10, 0.15\}$.

Analysis

Wave breaking is determined by looking at the propagation of the wave surface where $\gamma = 0.5$. The type of breaking waves seen in these simulations are known as a spilling breakers. Spilling breakers are characterized by crest destabilization and result in water

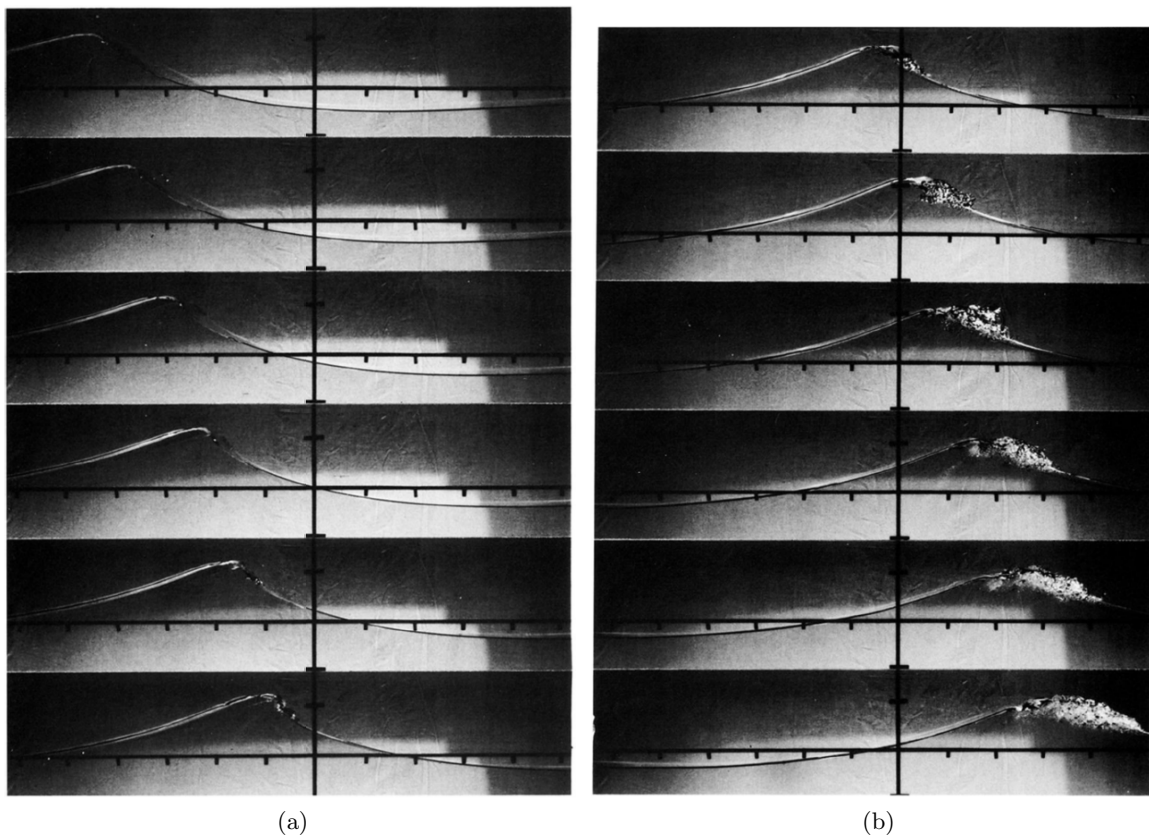


Figure 3.18: Example of spilling wave (Rapp and Melville, 1990)

spilling over the front of the wave. These waves will tend to have a frothy appearance near the crest. Gentle breaking of deep water waves, as reported by Melville (1982), is observed in cases where the steepness is above 0.05. The waves had a tendency to increase steepness until the wave surface profile resembled more of a triangle, then gentle breaking would occur at the crest and spill over the front face of the wave. Figure 3.19 shows the cases above and below the experimental breaking limit of 0.05. The evolution of the gentle breaking wave at a steepness of 0.06 is enclosed in a red box shown in figure 3.19. The crest of the wave becomes pointed and spills over the front of the wave. Table 3.8 shows a summary of the results.

Steepness X	0.03	0.04	0.05	0.06	0.07	0.10	0.15
Breaking	NO	NO	Minimal	Gentle	Gentle	Break	Break

Table 3.8: Wave steepness parameters

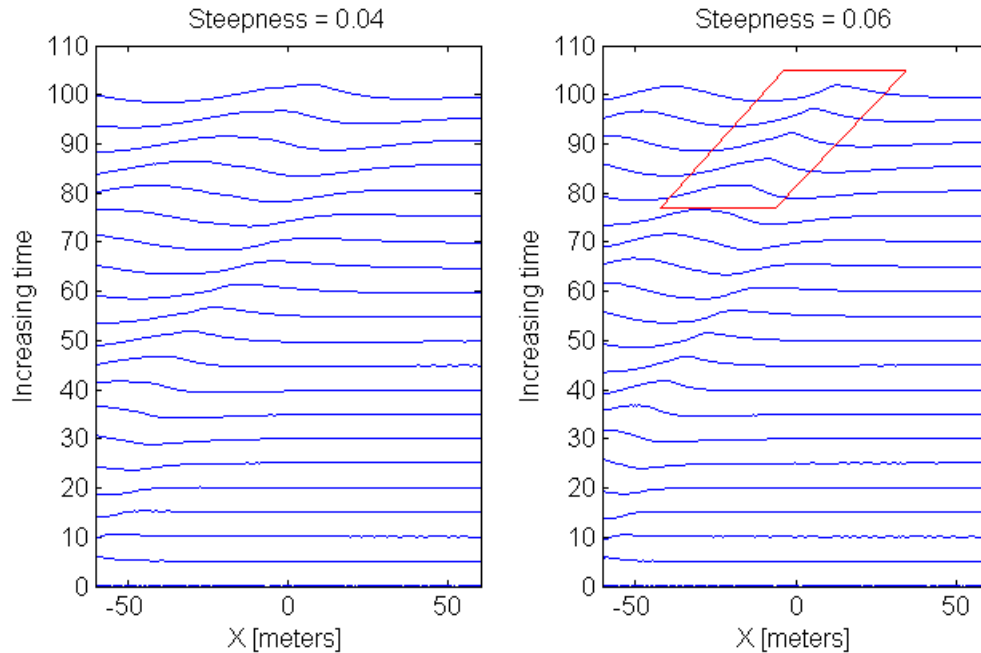


Figure 3.19: Waterfall plots of cases above and below experimental breaking limit for deep water spilling breakers

3.4.3 Uniform Grid Spacing Variation

The accurate propagation of wave form is dependent on grid spacing. This study looks at varying uniform grid spacings and compares the results against each other to reveal any inconsistencies. As with the previous studies, high amplitude sea states 5 and 6 are the basis for the incoming waves. The computation times are also compared because the required CPU time is always a consideration in CFD.

Grids

The grids used in this study are based on previous meshes with uniform structured cells in the region of wave surface propagation and unstructured cells below the water surface. These grids are 240 meters long and 100 meters deep. Five spacings are selected: 0.2m, 0.3m, 0.4m, 0.5m, 1.0m.

Analysis

Table 3.9 shows that as the spacing is reduced, the computation time is increased. Figure 3.20 shows that a spacing of 0.4m implemented for a sea state of 5 is sufficiently convergent. This means approximately 164 grid points per wave length are used to propagate the waves. At a sea state of 5 the solution seems to be more sensitive to the grid because the results do not converge as quickly as the sea state 6 results. This is expected as it will take a higher fidelity grid to capture smaller wave lengths. At sea state 6, the solution is relatively convergent with a spacing of 0.5m; showing that larger spacings can be used to propagate longer wave lengths.

Points per wave length $\Delta x/\lambda$	325	216	162	130	65
Time [hours]	19	6	4	3	1

Table 3.9: CPU time for sea state 5 cases

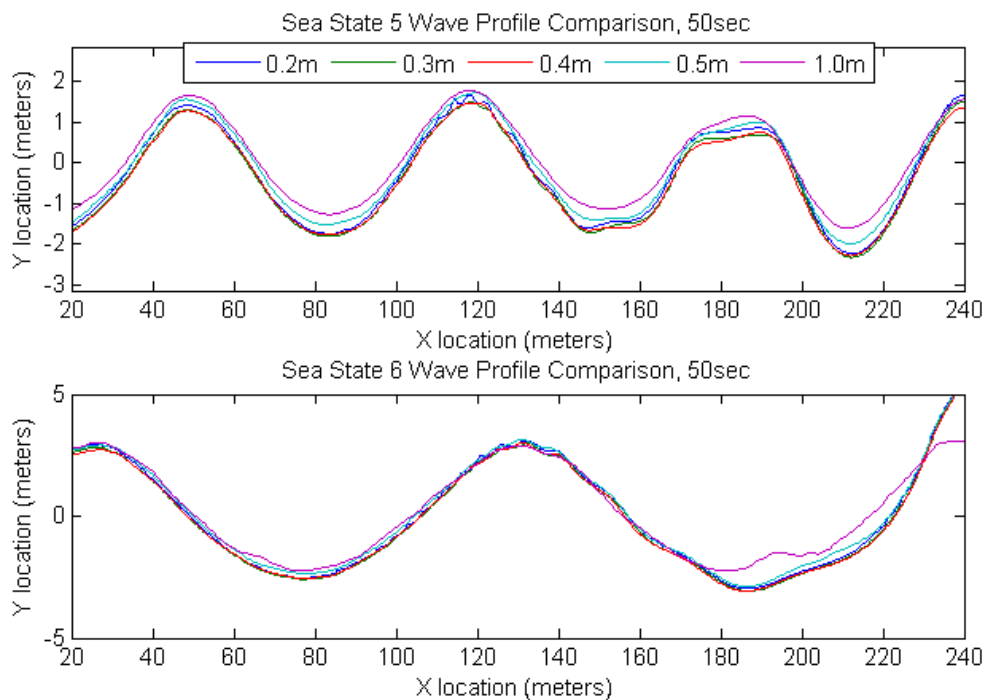


Figure 3.20: Grid spacing study

3.5 Sponge Layer

3.5.1 Wave Dissipation Cases

The purpose of this study is to characterize the effectiveness of the numerical sponge layer as different parameters are varied. An impulse surface wave is sent down a 2D wave tank and the reflection amplitude is measured. The length of the beach L and the maximum dissipation level $\nu_{d,max}$ are varied across a set of cases. The resulting reflection coefficient of each case is plotted to determine the character of the beach. The parameters, $\{\nu_{d,max}\} = \{1, 2, 4, 6, 10, 100, 1000\}$ and $\{L\} = \{2, 4, 6, 8\}$, are used to form a test matrix of simulations so that the performance and behavior of the beach can be characterized. The input wave impulse in all test cases has an amplitude of 8cm and a wave length of 1m.

Grid

The mesh is fully structured with no cell expansion in the region of wave surface propagation. In an actual application, the cells would be stretched in the area of the beach to minimize the reflections further. Figure 3.21 shows one end of the wave basin. The mesh is 20m long and allows a water depth of 60cm.

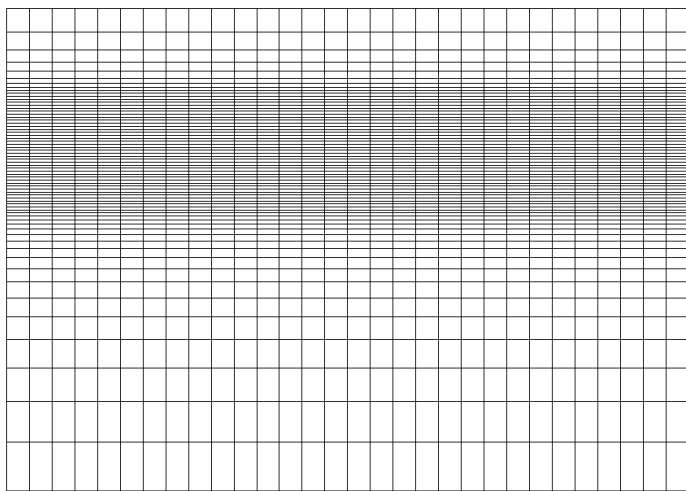


Figure 3.21: Section of wave tank mesh

Boundary Conditions

The boundary conditions are initially set as shown in table 3.10. The simulation is run for 6 seconds to generate the wave impulse which is a wave train consisting of 3 regular surface waves. The Left boundary condition is then switched to be advective for velocity and zero gradient for gamma.

Boundary	Pressure	Velocity	Gamma
Left (time \leq 6s)	Zero Gradient	Deep Water Wave	2nd Order Stokes Surface
Left (time $>$ 6s)	Zero Gradient	Advective	ZeroGradient
Right	Total Pressure	Advective	Zero Gradient
Top	Zero Gradient	Pressure I/O Velocity	Inlet Outlet
Bottom	Zero Gradient	Slip	Zero Gradient

Table 3.10: Wave basin boundary conditions

Analysis

The incoming and reflected wave amplitudes, A_i and A_r respectively, are sampled in ranges of time and space by taking the maximum wave amplitude in the chosen ranges. The results are plotted on waterfall diagrams to ensure the reflected wave is chosen correctly. The reflection coefficient is calculated as $R = A_r/A_i$ and plotted as a function of $\nu_{d,max}$ and L . Figure 3.22 shows that as the beach length is increased reflections are reduced regardless of the dissipation constant $\nu_{d,max}$. However, $\nu_{d,max}$ can be varied to make the sponge layer more efficient for a given beach length.

The effect of adding the beach can be further understood by examining the waterfall plots shown in figure 3.23. The case without a sponge layer shows a lot of reflections. The first reflection is due to the initial transient induced by the wave maker. This initial transient propagates quickly and reflects before the wave train hits the right boundary. The wave train then hits the boundary and reflects back into the domain. The calculated reflection coefficient for this case is relatively high at a value of 0.92. Therefore, the advective boundary condition has effectively transmitted about 8% of the wave energy out of the domain. The cases with sponge layers in figures 3.23b and 3.23c show that the dissipation model can be quite effective if the parameters are tuned correctly. Picking a higher $\nu_{d,max}$ has the effect of dissipating energy more rapidly. However, if the sponge layer length L is

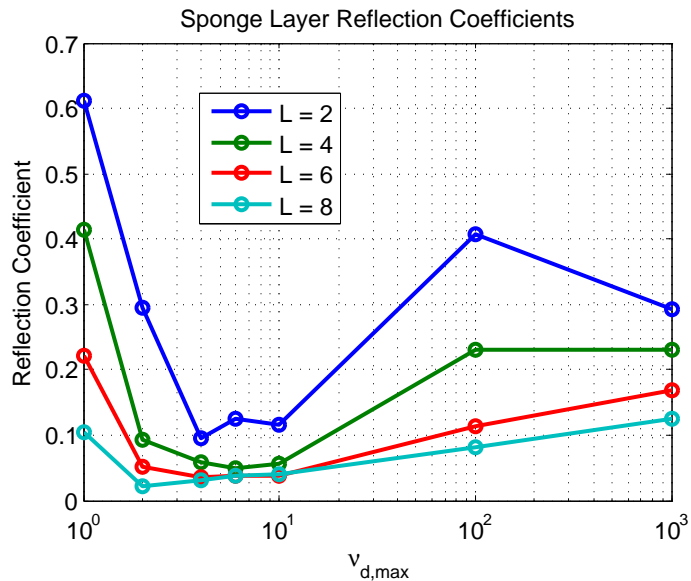


Figure 3.22: Reflection coefficients

too short, waves can reflect from the sponge layer itself. It is also interesting to observe that the higher dissipation rate also restratifies the surface elevation more quickly.

3.5.2 Wave Dissipation with Expanded Grid Cells

The effect of expanding the cells in the direction of wave propagation can increase the dissipation of a wave. In this study various beach lengths are tested as the parameter $\nu_{d,max}$ is varied. A non-uniform mesh as shown in figure 3.24 is added to the outlet end of a mesh. The sponge layer is active only in the region of the non-uniform cells. The waves propagate in a 20m region of uniform cells and are dissipated in the expanded region of the mesh. The waves are generated for 6 seconds and the wave maker is turned off as in the previous study.

Grid

The expansion ratio is kept constant at 1.1 and the beach lengths are set as $\{L\} = \{2.000033, 4.367271, 6.579761, 8.890062\}$. Figure 3.24 shows the region of the sponge layer with expanded cells.

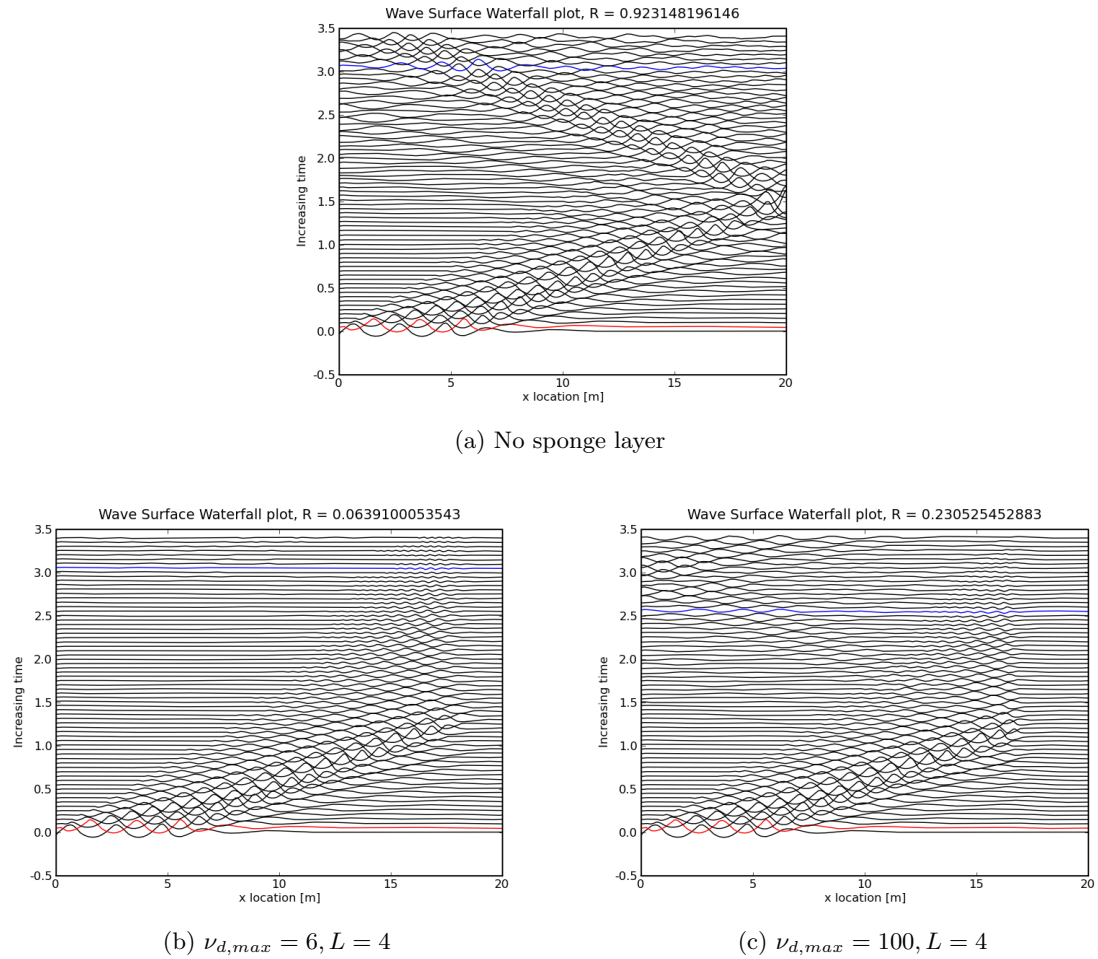


Figure 3.23: Water fall plots showing cases of varying beach parameters and no sponge layer

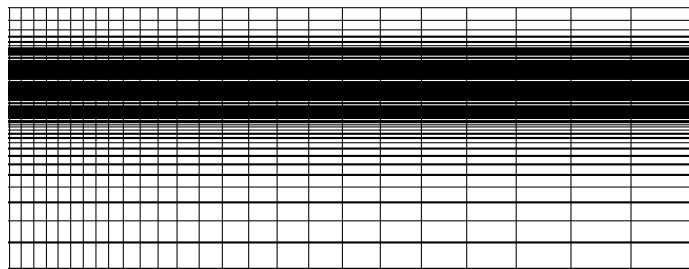


Figure 3.24: Region of mesh with active sponge layer

Boundary Conditions

The boundary conditions for this set of simulations is shown in table 3.10. A wave impulse is generated for 6 seconds and the wave maker boundary condition is switched to an advective

type.

Analysis

The reflection coefficient, R , is calculated for each case and is plotted in figure 3.25. In general, the graded beach made a drastic improvement in the dissipation of waves when compared with the results of the previous case. Figure 3.25 shows that the reflection coefficient curves collapse onto each other quickly as the beach length is increased when $\nu_{d,max} < 10$. The ideal range for $\nu_{d,max}$ seems to be in the range of 4 to 10. This study shows that a beach to wave length ratio of 4 will most effectively dissipate energy from surface waves if the dissipation constant is set correctly. This study has shown that wave reflections can be reduced to less than 5% of the incoming wave amplitudes using the the currently implemented methods.

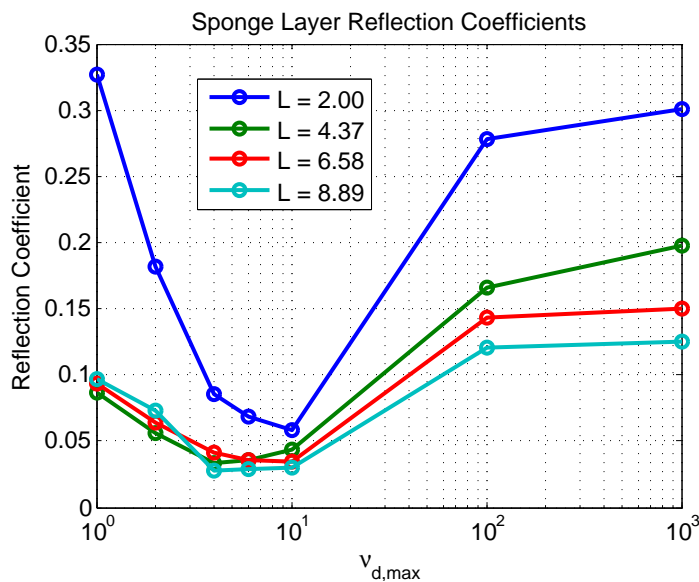


Figure 3.25: Reflection coefficient along constant beach lengths with graded mesh in sponge layer zone

3.6 Wave Slap Loads

3.6.1 Scaling of Impact Loads

The purpose of this study is to examine how well impact loads can scale to larger geometries. Experiments that are conducted to study ship hydrodynamics are typically around 1/25 scale. The results for a wave-slap experiment are scaled using the scale ratio. To examine wave-slap scaling effects a 2D dam break case is scaled 1, 10, 20, and 50 times. The maximum pressure on the front face of the block, indicated in figure 3.26a, is recorded at each time step. The pressure coefficient is then calculated over time and the data across the set of cases is compared to see how impact loads scale. It is assumed that the pressure coefficients across the set of cases should be equal, ie. $C_{p,1} = C_{p,2}$. A typical flow evolution is shown in figure 3.26b.

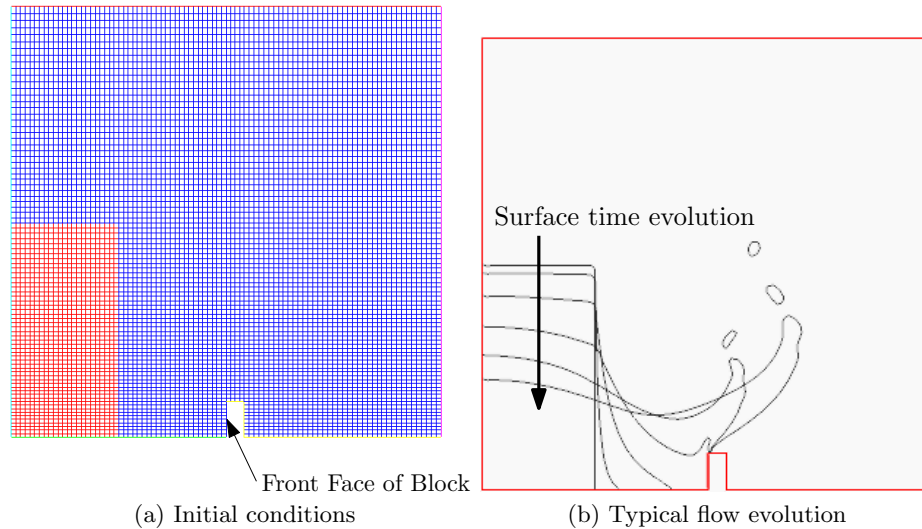


Figure 3.26: Dam break case

Grids

The grids for each case are scaled from the original geometry shown in figure 3.26a.

Analysis

The pressure coefficient for each case is calculated as $C_p = \frac{p}{\frac{1}{2}\rho U^2}$. The velocity scale is taken as $U = \sqrt{gh}$, where g is gravity and h is height of the initial water column. The time

is then non-dimensionalized by the initial impact time, t_{impact} , as $t^* \equiv t/t_{impact}$. Figure 3.27 shows that the pressure coefficient scales fairly well with respect to the original scale and overall the results are consistent showing the robustness of the technique. Another way to compare the data is take the ratio $p_{max}/p_{max,original}$ to obtain a scaled impact pressure ratio and then correlate to the geometry scale. Table 3.11 shows the comparison between the pressure ratio versus geometry scale. It is interesting to see that the error is fairly consistent near a value 2% and encouraging that the error is quite small for a case scaled 50 times the original size.

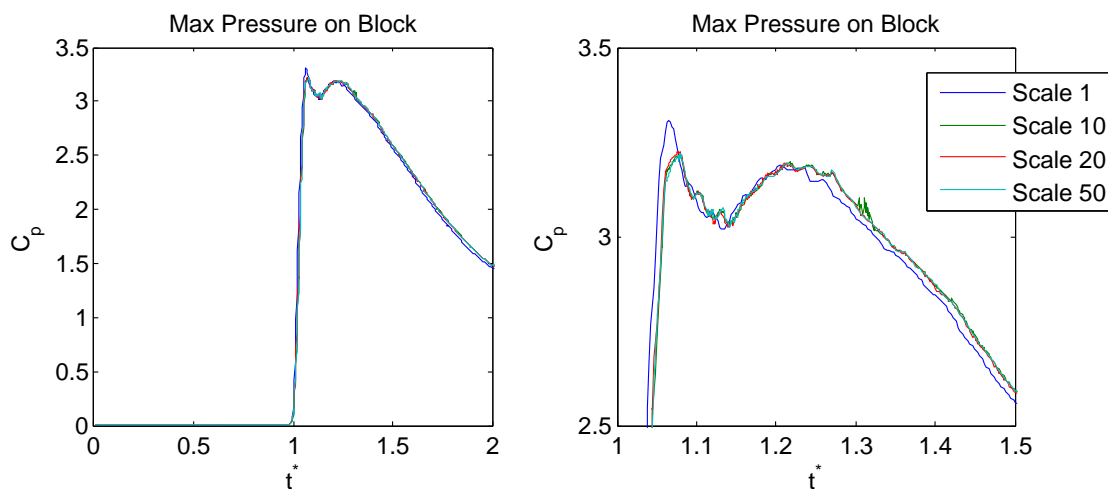


Figure 3.27: Dam break case - Pressure coefficient

Geometry Scale	$p_{max}/p_{max,original}$	Error %
1	1.0	-
10	9.8	2
20	19.6	2
50	48.9	2.2

Table 3.11: Scaling of impact pressure

Constant Re and Fr number

These simulations are based on the previous computations and use the same grids for each scale and the Fr and Re is assumed constant across the set of scaled cases. The Reynolds

number is held constant by varying the kinematic viscosity ν of water for each scaled case as $\nu_X = X\nu_0^{3/2}$. The results are shown in figure 3.28 and table 3.12. These results are slightly improved over the previous results. The original scale matches the C_p curve form better during the sampled time. Again the impact pressure ratios have a consistent error of 2% across the scaled cases.

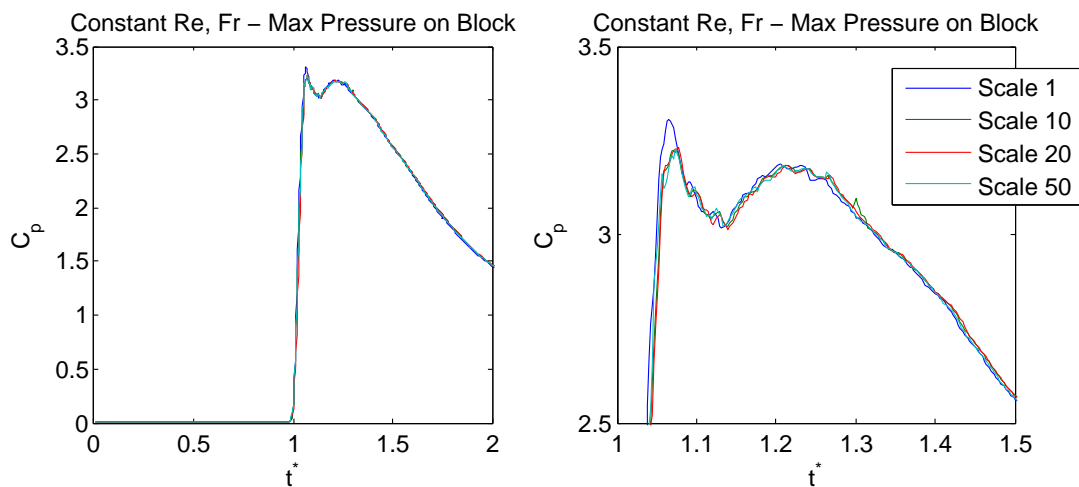


Figure 3.28: Dam break case with constant Re, Fr

Scale	$p_{max}/p_{max,original}$	Error %
1	1.0	-
10	9.8	2
20	19.6	2
50	49	2

Table 3.12: Scaling of impact pressure with constant Re, Fr

3.6.2 Impact Load Grid Dependency

This study looks at the influence of grid spacing on maximum impact pressure and pressure evolution. The dam break case scaled 50 times is the basis for all meshes.

Uniform Spacing

The grids used in this study have uniform point spacing in the computational domain. The results in figure 3.29 show that as the fidelity of the model is increased, higher pressures are observed. The work done by Greco et al. (2006), indicated that the initial impact load peak has a very short duration on the order of 10^{-5} seconds. This initial impact induces very high pressures. At the moment of impact in the highest fidelity case shown here, the time step was on the order of $8(10^{-4})$ seconds. Using a grid that has high fidelity across the entire domain is very computationally expensive and unnecessary in many cases. The main reason to use uniform grid spacing is to ensure the consistent propagation of the free-surface. Table 3.13 shows the impact time of each case.

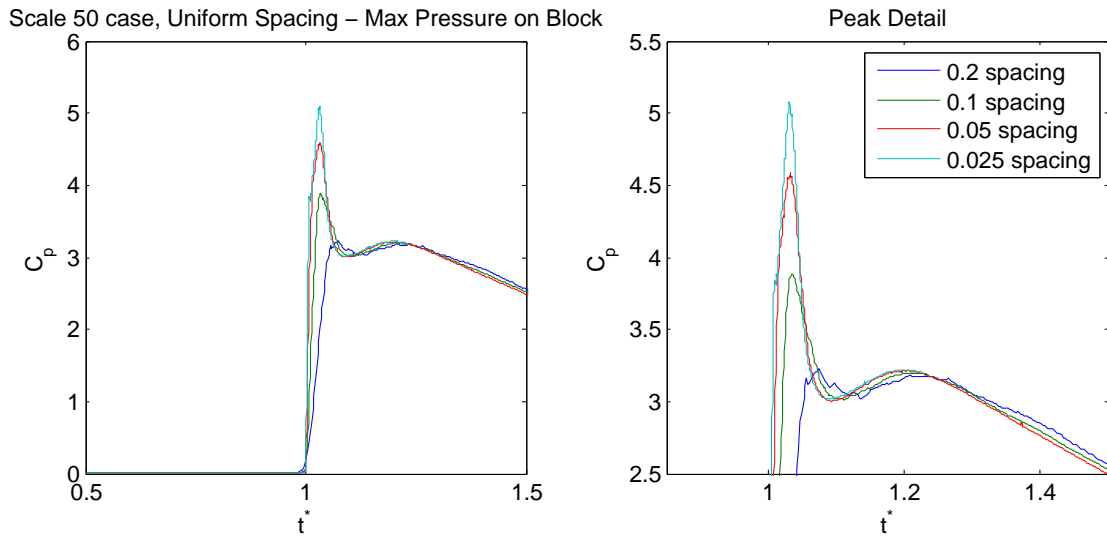


Figure 3.29: Dam break, uniform grid spacing

Spacing [m]	0.2	0.1	0.05	0.025
Impact time [s]	0.8521	0.8721	0.8739	0.8761

Table 3.13: Impact times

Graded Spacing

The purpose of this study is to try to resolve the initial impact pressure peak better and get solution convergence. It is also desirable to capture and discern the acoustic and blunt impact phases to study the phenomena shown by Greco et al. (2006). Graded meshes are used so that very high fidelity near wall spacing is obtained and computation time is reduced compared with using a uniform spacing across the domain. Figure 3.30 shows the graded mesh near the block where pressure data is taken. This will reduce the time step as the water approaches the block and resolve higher pressures. Figure 3.31 shows the effect on the pressure coefficient of adding higher resolution near the block. Higher pressures, one order of magnitude above the original results, are captured with the finest mesh. This can be considered the acoustic impact phase. The time step during the initial impact was reduced by an order to about $9(10^{-5})$ seconds. The blunt impact phase follows immediately and is on the order of $C_p \approx 3$. Table 3.14 shows the comparison of maximum pressure across the set of cases. The time of initial impact is also affected by grading the mesh as shown in table 3.14. The difference is not much but still shows the propagation is affected by grading the mesh as the results do not converge with the current set of meshes.

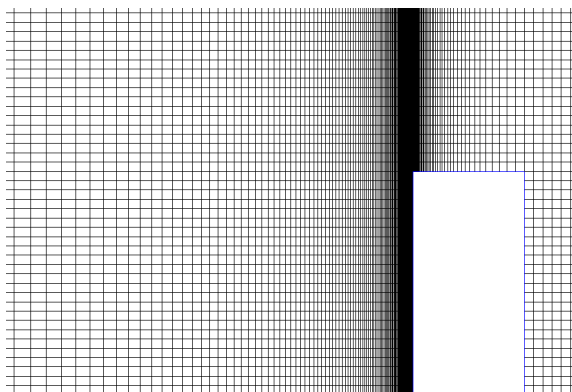


Figure 3.30: Dam break, graded mesh near block

Near Wall Spacing [m]	0.2 (not graded)	0.01	0.005	0.0025
Time of Impact [s]	0.8521	0.8757	0.8815	0.8651
Max Pressure [Pa]	2.3e5	4.2e5	7.1e5	1.1e6

Table 3.14: Impact times

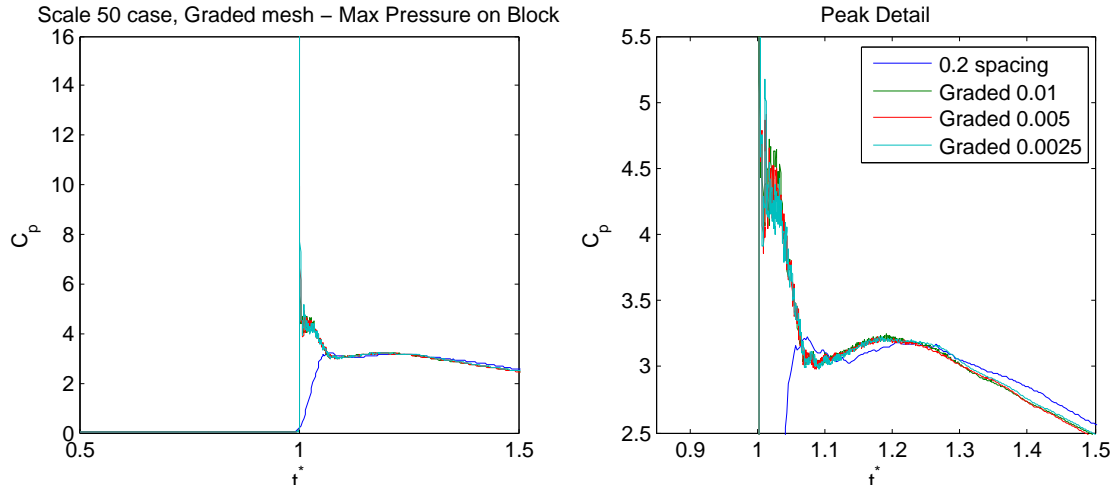


Figure 3.31: Dam break, graded mesh

3.6.3 Wave Loads on a Fixed Structure

This is a simulation of a fixed 2D block in regular wave field. This is a representation of an experiment done at NSW Carderock, however the EFD data was not available for comparison. The wave impact loads are measured using pressure probes on the front face of the block. The main purpose of this simulation is to accurately predict wave impacts. A schematic of the problem is shown in figure 3.32.

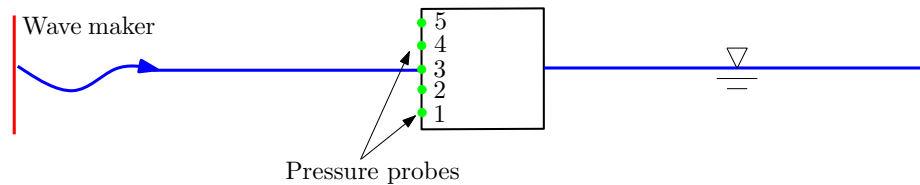


Figure 3.32: Wave-slap problem schematic

Grids

The mesh is shown in figure 3.33. The wave maker is on the left of the domain so a finer mesh is used in this region up to the front face of the block. After the block, the cells are stretched to save computation time and dissipate energy from the waves so reflections will be minimized.

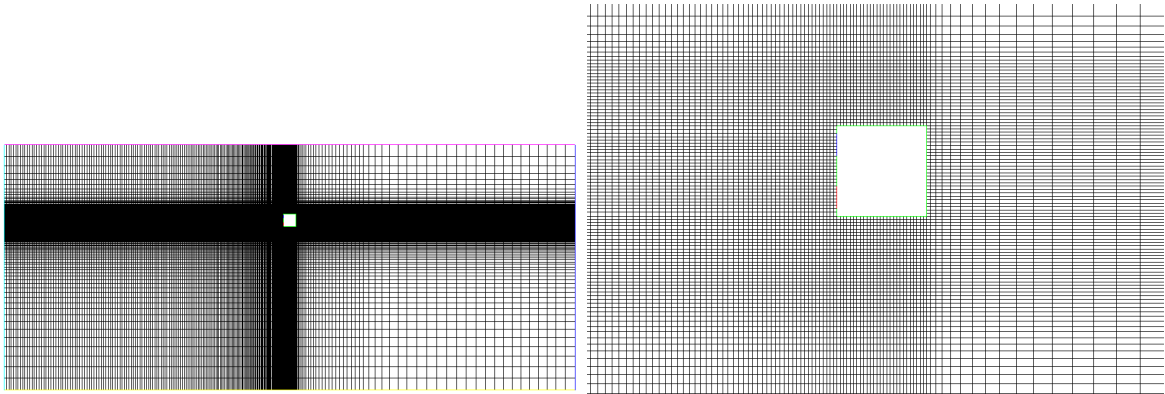


Figure 3.33: Overall and close-up views of the fixed block mesh

Boundary Conditions

The boundary conditions used in this simulation is shown in table 3.15. Regular waves are generated at the left boundary for the entire duration of the simulation.

Boundary	Pressure	Velocity	Gamma
Left	Zero Gradient	Deep Water Wave	2nd Order Stokes Surface
Right	Total Pressure	Zero Gradient	Zero Gradient
Top	Zero Gradient	pressureInletOutletVelocity	Inlet Outlet
Bottom	Zero Gradient	Slip	Zero Gradient
Block	Zero Gradient	No Slip	Zero Gradient

Table 3.15: Boundary conditions of fixed structure wave impact case

Analysis

Figure 3.34 shows the free-surface evolution as the wave hits the block. At 6.20 seconds, the wave pours over the top of the block and breaks. At about that moment the highest pressures are seen on the front face of the block shown in figure 3.35. One of the main advantages of using a non-linear code is that effects, such as wave breaking and flow separation, can be resolved. This example demonstrates how the wave model can be used to estimate the wave-slap pressures on a fixed structure.

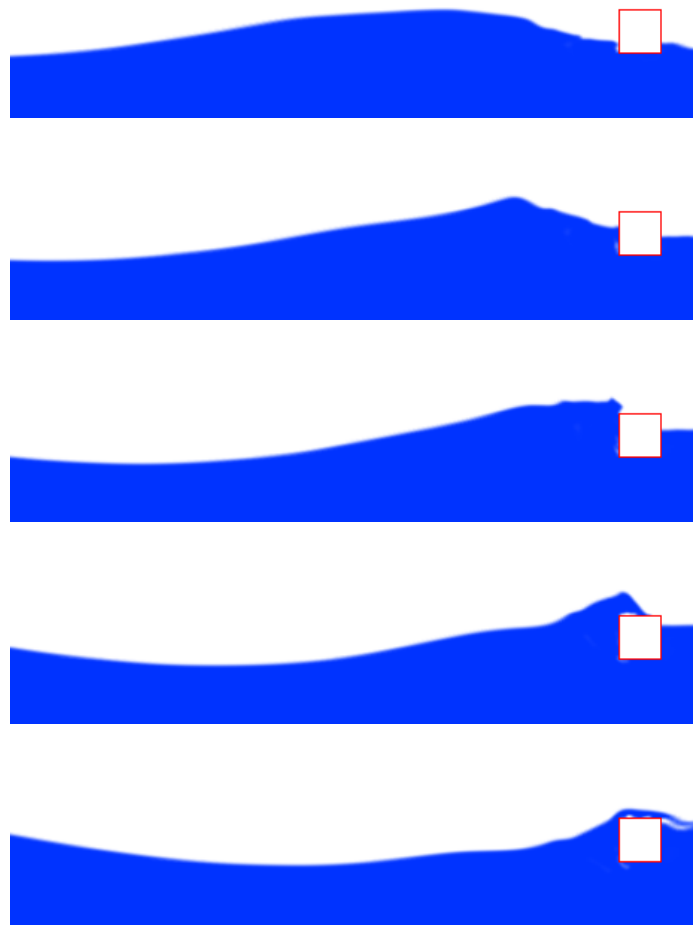


Figure 3.34: Wave impact flow evolution

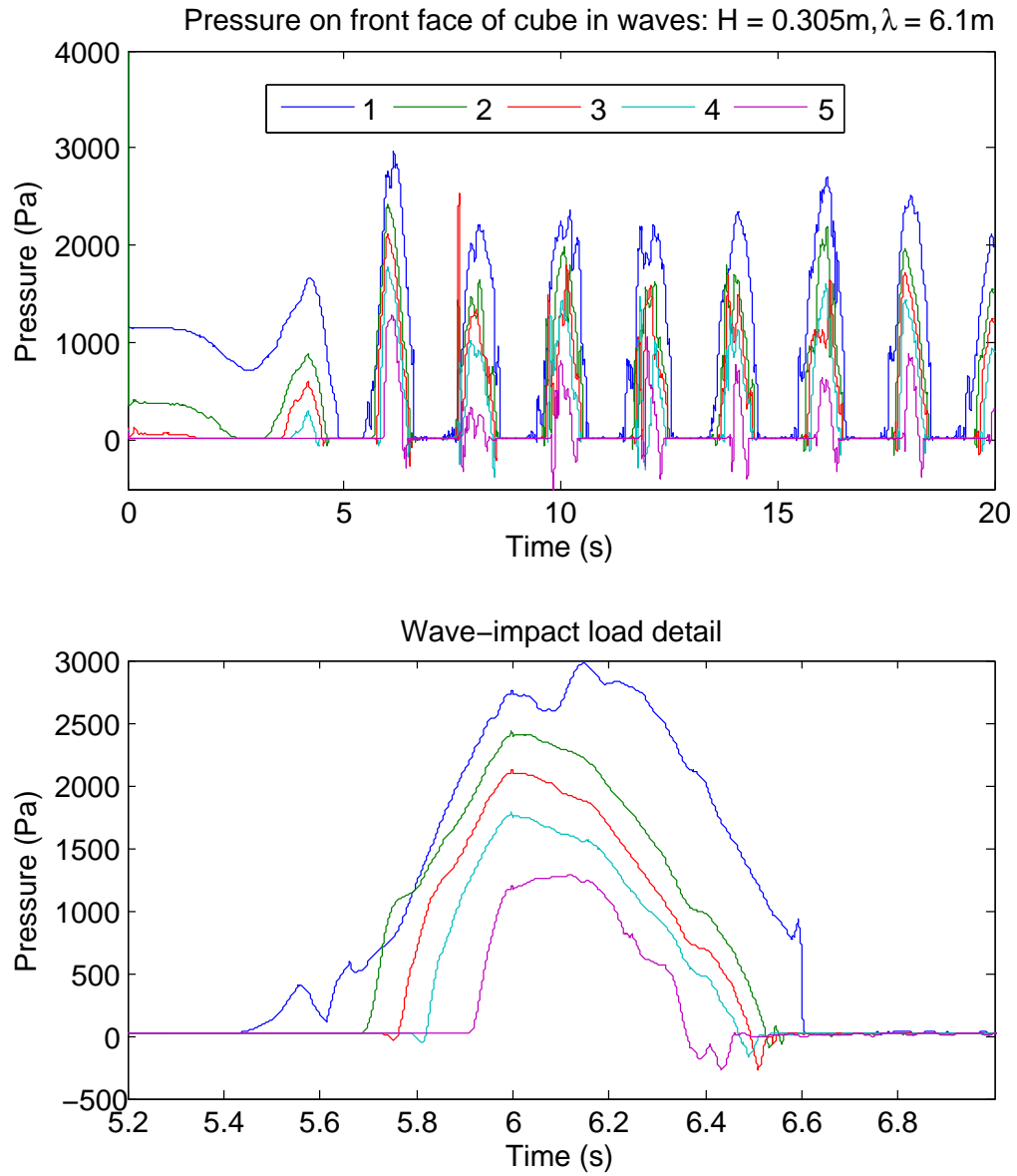


Figure 3.35: Impact pressure

Chapter 4

Summary

The components of a CFD physics-based seakeeping model have been developed and tested using OpenFOAM. The main components of this model were shown to be:

- 6DOF Motion
 - Mesh Motion
- Free Surface Models
 - VOF Method
 - Wave Models
 - * Deep Water
 - * Shallow Water
 - Sponge Layer
- Viscous Hydrodynamics
 - Navier-Stokes
 - Turbulence Model

Each component of this seakeeping and wave impact model was tested and presented. The most important conclusions from each section are summarized in this chapter.

4.1 Prescribed Motion

Extensive use of dynamic meshing has been implemented in the respective computational models that require rigid-body motion. The prescribed cylinder motion case showed that mesh motion can be quite robust on simple geometry with small amplitude motions. The

ONRTH case demonstrated an application of mesh motion to a free-surface problem. The geometry in the ONRTH cases was relatively complex with high amplitude roll up to 30° . The flow fields in all the cases were captured well, however experimental data is still needed to confirm the results. Some perturbations were seen on the surface which could be due to the mesh motion. However, since these were small and local in nature they are not expected to affect the solution much. More studies of mesh motion with free-surface VOF should be performed to provide further understanding. It was also found that, in general, mesh motion is computationally expensive.

4.2 Free 1DOF Motion

Ship motions are the main component in any seakeeping code so this is critical to benchmark and test. The box barge cases used dynamic meshing coupled with a 6DOF solver to accomplish the motions. In general, these cases showed good agreement with experiment. The free-roll decay test showed that the natural frequency of a floating body can be predicted accurately with the currently implemented methods. The damping predicted by the simulations also agreed reasonably well with experiments, however there is room for improvement. The wave-excited motion case showed that floating body motions due to waves can be predicted well using OpenFOAM.

4.3 Wave Model

These studies focused on the verification and validation of a deep water wave maker boundary condition and the propagation of waves using VOF and RANS techniques. The criteria for a deep water wave, $\text{depth} > \lambda/2$, was confirmed by the basin depth dependency studies. This is important especially when high sea states are present because the computational domain must be deep enough to propagate the waves correctly. All of the deep water wave model tests used sea states 5 and 6 which represent typical wave heights used in seakeeping computations. The propagation of the waves was also studied using grids of different fidelities. These studies showed that the propagation of waves can converge in a set of meshes with the correct amount of resolution. The phenomena of deep water wave breaking was

also studied using the current computational model and the results agreed well with experiment. These studies have shown that the VOF and RANS techniques can propagate waves accurately and wave breaking phenomena can be predicted reasonably well. Future development and implementation of a wind model is also suggested to more accurately recreate high sea states.

4.4 Non-Reflecting Boundary

A numerical sponge layer was developed and tested with various beach parameters and grid spacing techniques. Wave reflections from the boundary were reduced below 5% of the incoming wave amplitude in the best cases. By expanding the cells in the beach region, the waves can be more effectively dissipated. The beach needs to be about 4 times the length of the longest wave length to get the most effective dissipation. Since the sponge layer is most effective at dissipating high frequencies it can be considered a low-pass filter. Further improvement of the advective boundary condition could allow shorter sponge layers to be used.

4.5 Wave Impact Loads

The dambreak case was used to study scaling effects and impact load grid dependency. These cases showed that impact pressure can be scaled using the geometry scale with an expected error of about 2%. These results confirm the current scaling methods used in experimental techniques. The impact load grid dependency study showed that very high spatial and temporal resolution is required to capture the initial high pressure spike during a wave impact. Depending on the objective of a simulation, this may or may not be required. During these simulations it was also shown that graded meshes can adversely affect the propagation of a free-surface when using a VOF method. This means that uniform meshes should be used in regions of surface propagation. In other words, the expansion ratio in all directions should be 1 in those regions. Near walls, boundary layers and impact loads may need to be accurately resolved so a graded mesh should be used in those areas. The wave impacts on a fixed structure case showed how the wave model can be applied to wave

impact problems. Experimental data is still required to confirm the results of the wave impact case.

4.6 Future Work

The main components of a seakeeping model have been developed, tested, and verified. The next step is to integrate all the components and rigorously test the complete model. This will allow computations to be performed that can predict ship behavior at sea and wave impact loads simultaneously. Further development of the non-reflecting boundary condition is also suggested so that the sponge layer length can be reduced. Specifically, this includes improving the advective boundary condition. Various limited DOF computations such as roll-heave and roll-pitch-heave would be useful to further validate the overall model. The wave model could be expanded to allow 2D irregular waves to be created using a known spectrum input. Development of an overset or chimera grid capability for OpenFOAM would dramatically enhance the flexibility of this model. This development could reduce CPU time and allow large amplitude simulations such as capsizing tests to be conducted.

Bibliography

- R. Beck, W. Cummins, J. Dalzell, P. Mandel, and W. Webster. *Principles of Naval Architecture Volume III*. Society of Naval Architects and Marine Engineers, 1989.
- R. Bhattacharyya. *Dynamics of Marine Vehicles*. John Wiley & Sons, Inc., 1978.
- Y. Cao, R. Beck, and W. Schultz. An absorbing beach for numerical simulations of nonlinear waves in a wave tank. In *8th International Workshop on Water Waves and Floating Bodies, St. John's, Canada*, 1993.
- P. M. Carrica, R. V. Wilson, R. W. Noack, and F. Stern. Ship motions using single-phase level set with dynamic overset grids. *Computers & Fluids*, 36(9):1415–1433, 2007.
- A. Clément. Coupling of two absorbing boundary conditions for 2d time-domain simulations of free surface gravity waves. *Journal of Computational Physics*, 126:139–151, 1996.
- M. Greco, M. Landrini, and O. Faltinsen. Impact flows and loads on ship-deck structures. *Journal of Fluids and Structures*, 19:251–275, 2006.
- C.-J. Huang, E.-C. Zhang, and J.-F. Lee. Numerical simulation of nonlinear viscous wave-fields generated by piston-type wavemaker. *Journal of Engineering Mechanics*, 124(10):1110–1120, 1998.
- K. Jung, K. Chang, and H. Jo. Viscous effect of the roll motion of a rectangular structure. *Journal of Engineering Mechanics*, 132:190–200, 2006.
- T. Kleefsman. *Water Impact Loading on Offshore Structures*. PhD thesis, University of Groningen, 2005.
- A. Lal and M. Elangovan. CFD simulation and validation of flap type wave-maker. *Proceedings of World Academy of Science, Engineering and Technology*, 36:76–82, 2008.
- Q. Ma, G. Wu, and R. E. Taylor. Finite element simulation of fully non-linear interaction between vertical cylinders and steep waves. part 1: methodology and numerical procedure. *International Journal for Numerical Methods in Fluids*, 36:265–285, 2001.
- S. Malenica and A. Korobkin. Some aspects of slamming calculations in seakeeping. In *9th International Conference on Numerical Ship Hydrodynamics*, 2007.
- W. Melville. The instability and breaking of deep-water waves. *Journal of Fluid Mechanics*, 115:165–185, 1982.
- M. Nobari and H. Naderan. A numerical study of flow past a cylinder with cross flow and inline oscillation. *Computers & Fluids*, 35:393–415, 2006.

- I. Orlanski. A simple boundary condition for unbounded hyperbolic flows. *Journal of Computational Physics*, 21(3):251–269, 1976.
- J. Park, M. Kim, and H. Miyata. Fully non-linear free-surface simulations by a 3D viscous numerical wave tank. *Int. J. Numer. Meth. Fluids*, 29:685–703, 1999.
- E. Paterson. Multiphase and free-surface flow simulations. 3rd OpenFOAM Workshop, July 2008.
- W. H. Press, S. A. Teukolsky, W. T. Vetterling, and B. P. Flannery. *Numerical Recipes in C*. Press Syndicate of the University of Cambridge, 1992.
- R. Rapp and W. Melville. Laboratory measurements of deep-water breaking waves. *Philosophical Transactions of the Royal Society of London. Series A, Mathematical and Physical Sciences*, 331(1622):735–800, June 1990.
- J. Romate. Absorbing boundary conditions for free surface waves. *Journal of Computational Physics*, 99:135–145, 1992.
- H. Rusche. *Computational Fluid Dynamics of Dispersed Two-Phase Flows at High Phase Fractions*. PhD thesis, University of London, 2002.
- T. Sarkar and D. Vassalos. A RANS-based technique for simulation of the flow near a rolling cylinder at the free surface. *Journal of Marine Science and Technology*, 5:66–77, 2000.
- Y. Sato, H. Miyata, and T. Sato. CFD simulation of 3-dimensional motion of a ship in waves: application to an advancing ship in regular heading waves. *Journal of Marine Science and Technology*, 4(3):108–116, 2000.
- K. Shibata and S. Koshizucka. Numerical analysis of shipping water impact on a deck using a particle method. *Ocean Engineering*, 34:585–593, 2007.
- J. G. Telste and W. F. Belknap. Potential flow forces and moments from selected ship flow codes in a set of numerical experiments. Technical report, Naval Surface Warfare Center, May 2008.
- O. Ubbink. *Numerical prediction of two fluid systems with sharp interfaces*. PhD thesis, University of London, 1997.
- H.-W. Wang, C.-J. Huang, and J. Wu. Simulation of a 3D numerical viscous wave tank. *Journal of Engineering Mechanics*, 133(7):761–772, 2007.
- R. V. Wilson, P. M. Carrica, and F. Stern. Unsteady RANS method for ship motions with application to roll for a surface combatant. *Computers & Fluids*, 35(5):501–524, 2006.